Birgit Six, BSc

Influence of Self-Assembling Monolayers on the Performance of Bulk Heterojunction Solar Cells

MASTERARBEIT

zur Erlangung des akademischen Grades

Diplom-Ingenieurin

Masterstudium Technische Chemie

eingereicht an der

Technischen Universität Graz

Betreuer

Assoc. Prof. DI Dr. Gregor Trimmel

Institut für Chemische Technologie von Materialien

Graz, November 2014

EIDESSTATTLICHE ERKLÄRUNG

AFFIDAVIT

Ich erkläre an Eides statt, dass ich die vorliegende Arbeit selbstständig verfasst, andere als die angegebenen Quellen/Hilfsmittel nicht benutzt, und die den benutzten Quellen wörtlich und inhaltlich entnommenen Stellen als solche kenntlich gemacht habe. Das in TUGRAZonline hochgeladene Textdokument ist mit der vorliegenden Masterarbeit identisch.

I declare that I have authored this thesis independently, that I have not used other than the declared sources/resources, and that I have explicitly indicated all material which has been quoted either literally or by content from the sources used. The text document uploaded to TUGRAZonline is identical to the present master's thesis.

Datum / Date

Unterschrift / Signature

ABSTRACT

Bulk heterojunction solar cells represent a promising technology in the area of organic photovoltaics. The photoactive material consists of a network of electron donor, for example, conjugated polymers, and an electron acceptor, usually fullerene derivates. A distinction is made between normal and inverse architecture, depending on whether the electrons are extracted by the back electrode or by the transparent electrode. Due to the layered structure, the adaption of the different energy levels of the materials used as well as the adhesion of them next to each other are important criteria for the efficiency of organic solar cells. Interfacial properties can be controlled and improved by the use of self-assembling monolayers (SAMs).

This thesis deals with the influence of SAMs on the characteristic parameters of solar cells. Therefore, benzoic acid, four para-substituted derivatives thereof and two organo-phosphonic acids are used.

The first part focusses on the normal architecture using vanadium oxide as hole transport layer. On the V_2O_5 layer the SAMs, benzoic acid and its derivates, are applied with two different techniques. The adhesion of these monolayers is verified with contact angle measurements of water and XPS-analyzes. The characterization of the solar cells is made by current-voltage measurements. In the second part, the inverted architecture is used with titanium oxide as electron transport layer. Two different PEDOT:PSS solutions as well as molybdenum oxide are used as hole transport layer. Here, too, the contact angle of water and XPS measurements are carried out for the analysis of the SAM layers. The solar cells are again characterized by current-voltage measurements.

KURFASSUNG

Bulk-Heterojunction Solarzellen stellen eine vielversprechende Technologieform im Bereich der organischen Photovoltaik dar. Das photoaktive Material besteht aus einem Netzwerk aus Elektronendonator, zum Beispiel konjugierte Polymere, und einem Elektronenakzeptor, meist Fullerenderivate. Man unterscheidet zwischen normaler und inverser Architektur, je nachdem, ob die Elektronen über die Rückseitenelektrode oder die transparente Elektrode abgeführt werden. Durch den schichtweisen Aufbau sind sowohl die Anpassung der einzelnen Energielevels der verwendeten Materialien sowie die Haftung dieser aneinander wichtige Kriterien für die Effizienz organischer Solarzellen. Die Grenzflächeneigenschaften können mittels selbst-organisierender Monolagen (SAMs) gesteuert und auch verbessert werden.

Diese Arbeit beschäftigt sich mit dem Einfluss von SAMs auf die charakteristischen Parameter von Solarzellen. Es werden hierfür Benzoesäure, vier para-substituierte Derivate der Benzoesäure und zwei Organo-Phosphonsäuren verwendet.

Der erste Teil befasst sich mit dem normalen Zellenaufbau und Vanadiumoxid als Lochtransportschicht. Auf die V_2O_5-Schicht werden als SAMs Benzoesäure und ihre Derivate mit zwei unterschiedlichen Techniken aufgetragen. Die Haftung dieser Monolagen wird mittels Kontaktwinkelmessung von Wasser und XPS-Analysen überprüft. Die Charakterisierung der Solarzellen erfolgt durch Strom-Spannungs-Messungen. Im zweiten Teil wird die inverse Architektur mit Titanoxid als Elektronentransportschicht verwendet. Als Lochtransportschicht werden zwei unterschiedliche PEDOT:PSS-Lösungen sowie Molybdänoxid verwendet. Neben der reinen Benzoesäure und ihren Derivaten werden zwei Phosphonsäuren eingesetzt. Auch hier werden neben dem Kontaktwinkel von Wasser, XPS-Messungen zur Analyse der SAM-Schicht durchgeführtt. Die Solarzellen werden wieder mit Strom-Spannungs-Messungen charakterisiert.

ACKNOWLEDGMENT

First of all, I want to thank my supervisor Assoc. Prof. DI Dr. Gregor Trimmel for giving me the possibility to work on this interesting and emerging topic and of course for his support during my master thesis.

Special thanks goes to DI Dr. Verena Harum for her support, suggestions and her patience with me. Furthermore, I want to thank our working group for the great teamwork and the friendly and enjoyable atmosphere.

I want to thank Ass. Prof. Dr. Thomas Griesser (Department Kunsstofftechnik, Montanuniversität Leoben) for the analysis of my samples via XPS.

Furthermore, I want to thank my colleagues at the institute, especially Birgit Ehmann for the coffee breaks, as well as all people I met during my study.

I want to thank all my friends for their support, the anytime welcome diversion and their motivation all over the time.

The deepest gratitude are due to my family, especially to my mom. Without you, this study would not have been possible! Thank You!

TABLE OF CONTENTS

1. INTRODUCTION

1.1. Electricity Generation

The impacts of climate change, caused by the steadily increasing utilization of fossil resources has started to a rethink of the society in terms of sustainability and green energy. Thereby, an important factor is the reduction of anthropogenic greenhouse gases. To reduce especially the energy-related carbon dioxide emissions, it is necessary to promote the spread of green energy sources and the public support of them.

According to the World Energy Outlook 2013, the world net electricity generation will increase in the IEO2013 Reference case from 20.2 trillion kWh in 2010 to 39.0 trillion kWh in 2040 (see Figure 1), whereby the largest growth will be located in the area of regenerative energies, especially the water and wind power sector. [1]

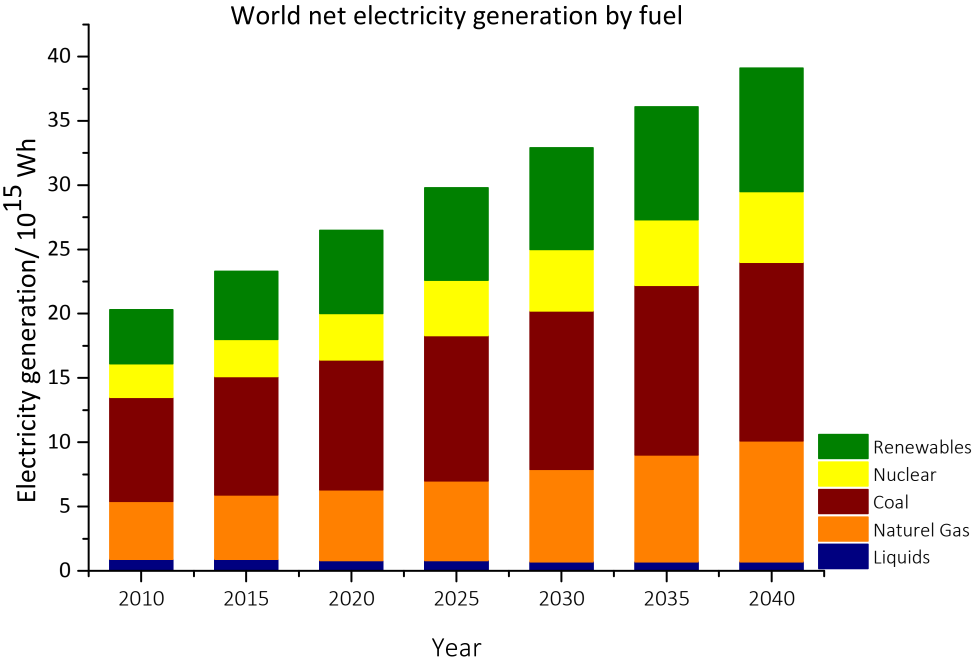

Figure 1: World net electricity generation by fuel (according to reference 1).

Today electricity from solar energy systems plays only a minor role worldwide, although the incident solar radiation supplies power of about 885 million TWh, which is 6200 times the economic primary energy consumption in 2008 and 4200 times in 2035 following the IEA´s Current Policies Scenario.[2]

Some European governments have launched feed-in-tariffs including, for example long-term agreements with renewable energy producers, to promote electricity generated from renewable sources.[1] So it is not surprising, that within 2012 the installed photovoltaic (PV) capacity in Europe is with 55% the fastest growing source.[3] The development of the European compared to the global PV installed capacity is shown in Figure 2.

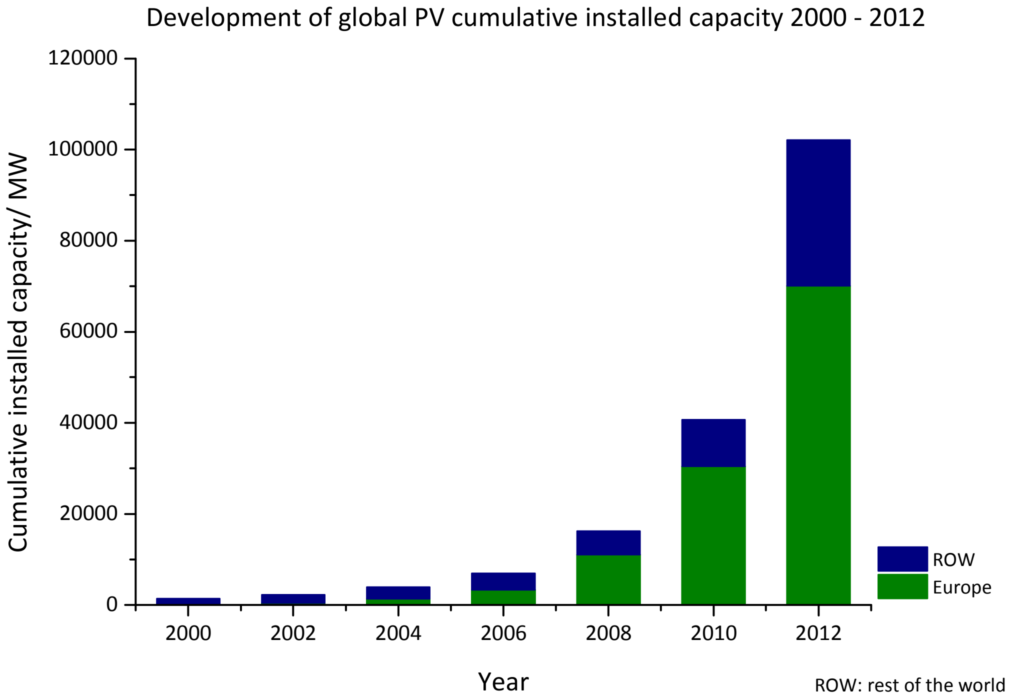

Figure 2: Development of the global PV cumulative installed capacity 2000–2012 (according to reference 3).

Electricity derived from solar energy will also play a major role outside Europe, as PV installations are more and more attractive to regions with a projected strong economic growth.[2] However, to promote and increase PV implementations it is still necessary to improve existing technologies.

1.2. Solar Cell Technology

In 1839, Alexandre E. Becquerel was the first scientist, who studied the influence of sunlight on the electrical properties of matter.[4] Until the first solar cell – as we know it – it still took more than 100 years. Only the explanation for the "*Conception of the Junction Transistor*" of William B. Shockley in 1949 provided the theoretical basis for solar cells used today.[5] In 1954, the scientists D. Chapin, C. Fuller and G. Pearson, working at the Bell Laboratories, built the first workable boron-doped silicon solar cell by connecting several cells together to a panel, which they called a "solar battery".[6]

At the beginning, the solar cells found application in aeronautics, but with the oil crisis in the 1970s came the first great interest in this emerging technology. Since this time, PV installations are also used for decentralized energy supply.[7]

Nowadays various types of solar cells are available. The widely used are silicon solar cells that are made of either crystalline or amorphous silicon. Former belong to the thick-film technology (first generation) and differ by a mono- or polycrystalline structure. Amorphous silicon solar cells are counted to the thin-film technology (second generation), which also includes semiconductor solar cells like cadmium telluride (CdTe) and copper indium gallium selenide (CIGS).[8] Furthermore, there are tandem solar cells and concentrator systems.[9]

Another emerging part of the solar cell technology is organic photovoltaic (OPV). There are various forms of organic solar cells: single layer, bilayer and bulk heterojunction (BHJ) solar cells. The latter architectures consist of an electron acceptor and electron donor (for detailed description see Chapter 2.1.).

According to *The Nikkei* in April 2011[10] Mitsubishi Chemicals produced an organic solar cell with a 9.2% conversion efficiency and in 2013, Heliatek®[11] presented its world record cell, consisting of small molecules, with 12% efficiency. This seems promising for the future of the OPV technology, but there is still a long way to commercial success, especially since there are rarely any long-term studies regarding durability and efficiency loss.

2. BASICS

2.1. Organic Photovoltaic

Although the OPV technology cannot replace solar cells of the first and second generation yet, there are definitely advantages in the use of organic semiconductors:[12,13]

- Easy process technology for example roll-to-roll process.
- Low material consumption because of the thin-film technology.
- Energy-saving and large scale production.
- Huge diversity of materials.

As mentioned above, the bilayer as well as the bulk heterojunction OPV devices consist of two different organic semiconductors to generate electricity; an electron-donating semiconductor such as unsaturated hydrocarbon compounds with a delocalized π-electron system and an electron acceptor at the other side, for instance fullerene derivates because of their high electron affinity.[12,13,14]

2.1.1. Operating Mode

In organic solar cells, the following operations are necessary to convert light into electricity (see Figure 3):[12,14]

a) Absorption of a photon and excitation of an electron to create a bound electron-hole pair, also called exciton.
b) Diffusion of the exciton to the interface of the electron affine semiconductor, where the dissociation of the electron-hole pair takes place.
c) Transport of the free charge carriers.
d) Collection of the charges through the respective electrodes.

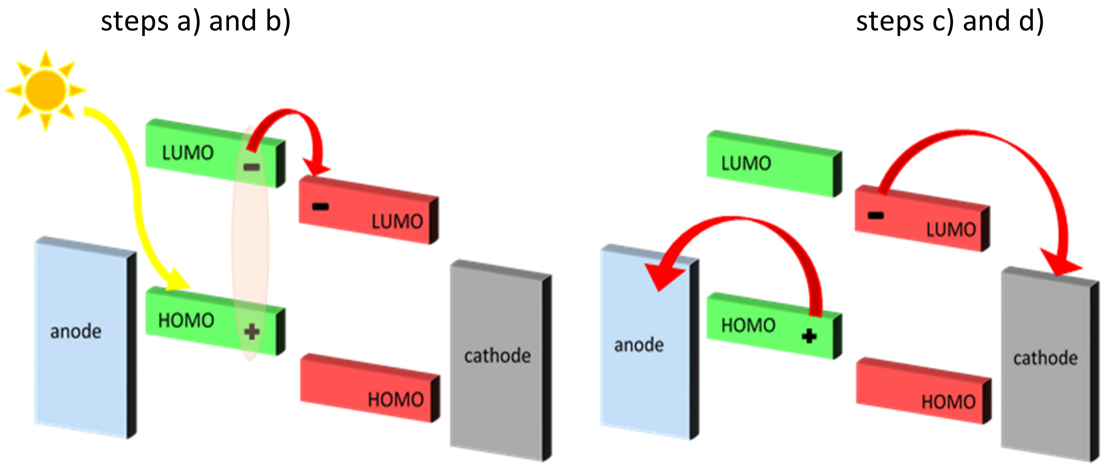

Figure 3: Conversion of light into electricity (according to reference 14).

The dissociation of the light-induced excitons is an important factor for the efficiency of organic solar cells (see Figure 3, step b). Therefore, a strong electric field, such as a donor-acceptor interface, is needed.[12] If the electron-hole pair gets to such an interface, a charge transfer takes place. The driving force for the transport of the free charge carriers is a gradient in the chemical potentials of the donor and acceptor.[12] The highest occupied molecular level (HOMO) of the donor and the lowest unoccupied molecular level (LUMO) of the acceptor determine this gradient.[12,14]

After dissociation of the electron-hole pair, the free charge carriers are collected from two different electrodes. Therefore, the electrons hop from one acceptor molecule to the next and the holes from donor molecule to donor molecule (see Figure 3, step c).[14] A transparent conducting oxide, which is matched to the HOMO of the donor polymer, captures the holes; the electrons are collected from a metal contact, whose work function fits the LUMO of the acceptor material (see Figure 3, step d).[14]

As mentioned above, there are several forms of arrangement of the organic materials, like bilayer and bulk heterojunctions (see Figure 4).[12-15] In the bilayer structure, the electron donor and electron acceptor materials are stacked on top of each other. A problem, which leads to a lower quantum efficiency, is the length of the exciton recombination that is usually between 10-20 nm.[14,15] Thus, only near the interface enough free charges can be produced.[14,15] The knowledge of this short distance and the discovery of the ultrafast electron transfer[16] resulted in the first bulk heterojunction solar cells, which were fabricated in the working group of A. J. Heeger.[17,18]

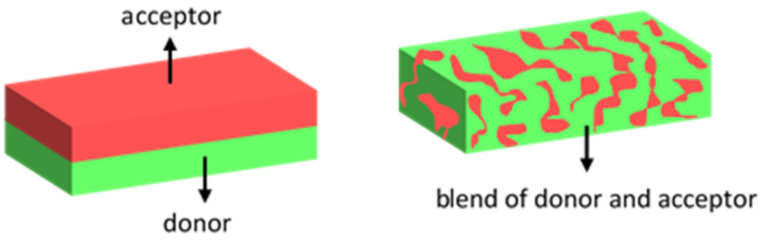

Figure 4: Bilayer and bulk heterojunction.

In the BHJ the donor and the acceptor build an interpenetrating network and so the required pathways for charge transport through the active material are given.[12,14,19] Moreover, the interfacial area between donor and acceptor is increased due to the percolated network, which leads to a higher efficiency. Additionally, there must be a sufficient contact area between the active materials and the corresponding electrodes.[14] Nevertheless, there are also separated domains and so there is still a loss of free charge carriers. To ensure the transport of the holes and the electrons through the blend to the right electrodes, it is necessary, that they have different work functions.[12,13,14,15]

2.1.2. Parameters of Solar Cell Devices

Solar cells are characterized by current-voltage (IV) characteristics, which are measured in the dark and under illumination. To ensure a standardized procedure, the power input is usually 1000 W/m² and the spectral intensity distribution fits to a solar zenith angle of 48.19°, also called air mass 1.5 spectrum (see Figure 5).[20]

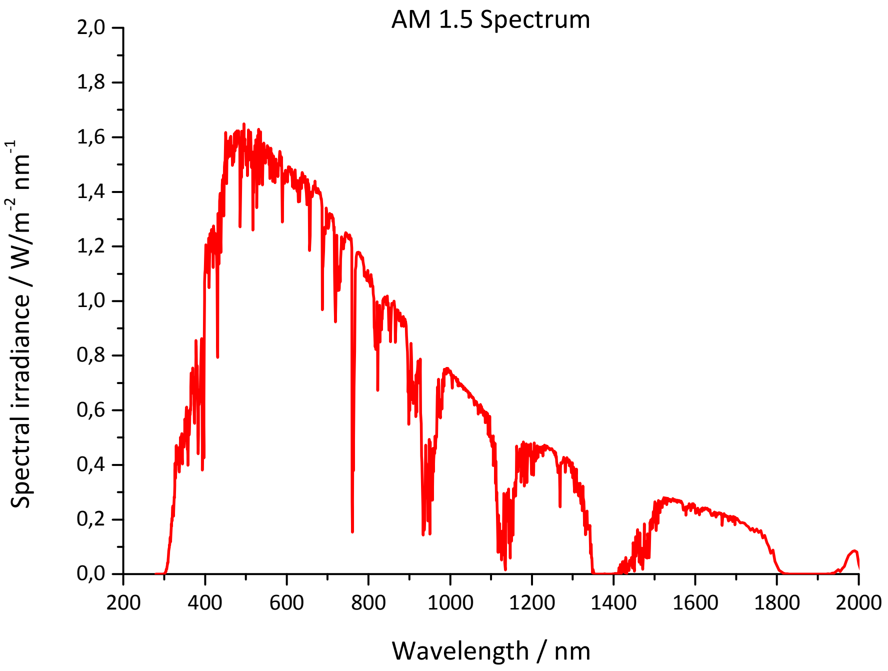

Figure 5: AM 1.5 Spectrum (according to reference 20).

To describe the efficiency of a photovoltaic device the following characteristics are used:

- The Open Circuit Voltage V_{OC}

The V_{OC} is the available voltage at zero current, which is determined by various factors: the difference between the HOMO level of the donor[12,14,21,22]and the LUMO level of the acceptor,[12,14,22] the work function of the electrodes,[12,14] the morphology of the photoactive layer[19,23], as well as the buffer layers.[24,25]

- The Short Circuit Current I_{SC}

The I_{SC} is the current density at zero voltage. It depends on the mobility of the free charge carriers and the photo-induced charge density, which are device parameters.[12,14,15,19,24] The I_{SC} is also influenced by the nanomorphology.[19,26]

- Fill Factor *FF*

The holes and electrons arriving at the respective electrodes define the fill factor.[12,15,22] The ratio of the maximum power to the short circuit current and the open circuit voltage define the FF:[13]

$$\mathrm{FF} = \frac{\mathrm{I_{MPP}} * \mathrm{V_{MPP}}}{\mathrm{I_{SC}} * \mathrm{V_{OC}}}$$

- Power Conversion Efficiency *PCE* (η)

The PCE is the ratio between the generated electrical energy and the incident light power.[12,15]

$$\eta = \frac{P_{OUT}}{P_{IN}} = \frac{V_{OC} * I_{SC} * FF}{P_{IN}}$$

Figure 6 shows the typical IV-characteristics of an OPV device, with the crucial parameters plotted.

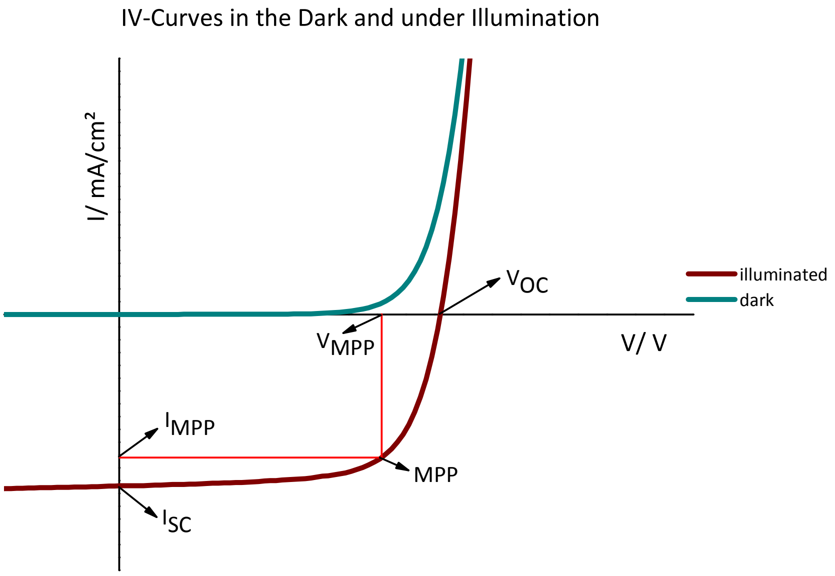

Figure 6: IV-Curves in the dark and under illumination (according to references 12 and 13).

2.1.3. Architecture of an OPV Device

Beside the different texture of the photoactive layer, there are two kinds of device architectures (see Figure 7):[13,19,22,] the normal device, in which the holes are collected through a transparent conductive electrode and the inverted architecture, where the electrons are captured through this transparent contact. Both architectures include a glass substrate coated with conducting oxides like indium tin oxide (ITO).[12,13,22,27] ITO is a wide band gap semiconductor and possesses a high transmittance in the visible and near-infrared field of the electromagnetic spectrum.[27]

In the normal device architecture, a hole transport layer is deposited on top of the ITO coating. Generally a hole-conducting layer, consisting of poly(3,4-ethylenedioxythiophene) doped with a polystyrene sulfonate (PEDOT:PSS)[28] is used, but also metal oxides with a high work function, such as V_2O_5 are utilized.[29] As a result, the quantum efficiency is enhanced because of the decrease of charge carrier recombination at the interface to the photoactive layer.[29] The active film is sandwiched between this HTL and the metal contact for collecting electrons. This electrode consists of a metal with a low work function, for example aluminum.[30]

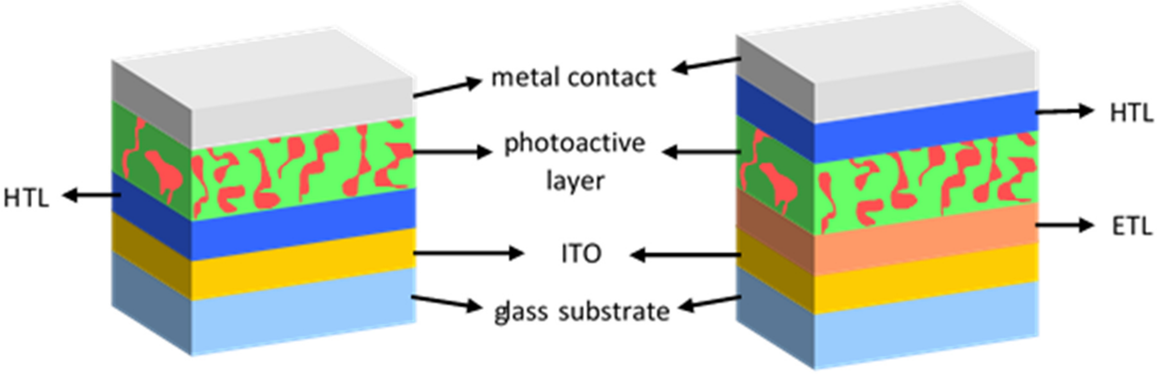

Figure 7: Normal device (left) and inverted architecture (right).

The architecture of inverted organic solar cells is shown in Figure 7. ITO is not a suitable material for collecting electrons because of its high work function.[31] An electron transport layer such as TiO_X has to be inserted.[30-32] It is well suited for blocking holes because of its low HOMO level and sensitive for electrons because of its LUMO level.[31,32] The HTL in inverted devices is the same as for the normal architecture either PEDOT:PSS or a transition metal oxide.[31,32] A high work function metal like silver or gold is used for the metal electrode.[32,33]

2.1.4. P3HT:PCBM based Solar Cells

In addition to a high absorption of sunlight, organic semiconductors need the ability to generate many free charge carriers and to transport them to the respective electrodes.[12,14,34] An important point for increased charge carrier transport is a certain crystallinity of the percolated network of the two phases.[19,34,35]

Poly-(3-hexylthiophene) (P3HT) is well suited as an electron donor in combination with [6,6]-phenyl C_{61} butyric acid methyl ester (PCBM) as electron acceptor.[12,14,34,35] The chemical structures of both compounds are shown in Figure 8.

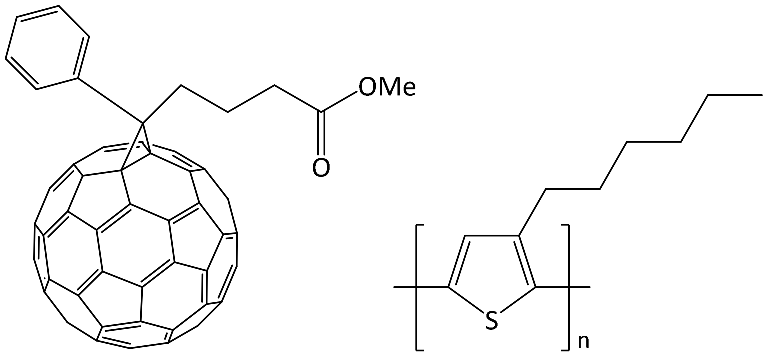

Figure 8: Chemical structure of PCBM (left) and P3HT (right).

These two substances have interesting intrinsic properties. P3HT for example forms a microcrystalline structure[35,36] and has a high mobility (0.05–0.1 $cm^2\ V^{-1}\ s^{-1}$)[37] for efficient hole transport. PCBM possesses an electron mobility[38] of $2 * 10^{-3}\ cm^2\ V^{-1}\ s^{-1}$ and it has an active influence on the crystallizing process of P3HT.[39] Since for an optimal solar cell efficiency the LUMO levels between donor and acceptor should be 0.3 eV apart for efficient charge separation,[21] P3HT:PCBM is suitable because of a difference of 0.3-0.4 eV.[29,30,40-44]

The HOMO level and LUMO level of P3HT are around 4.9–5.1 eV and 3.0–3.3 eV, respectively.[29,30,40-44]This results in a band gap of around 1.9 eV. The HOMO level of PCBM is in the range of 5.9-6.1 eV and the LUMO level of PCBM is located at 3.6-3.7 eV.[39-44]

Different parameters such as the ratio between donor and acceptor, the used solvent, processing conditions and post-treatment such as thermal annealing have big influences on the morphology.[35,41,43,44] Heeger et al.[44] found out, that an optimal ratio between P3HT and PCBM is 1.0 to 0.8 w%. Furthermore, thermal annealing by temperatures above 120 °C for around 30 minutes results in an increased cell efficiency.

Although polymers with enhanced electrical and optical properties are available nowadays, P3HT:PCBM is still used as a reference system due to its well-studied properties.[12,14, 29,30,34-44]

2.2. Self-Assembling Monolayers

Surfactant molecules are well-known representatives of molecules, which are able to form monolayers. Other important substances of this chemical class are thiols[45,46], trichlorosilanes[47-49], phosphonic acids[50-52] and carboxylic acids.[46,52-61] These molecules are distinguished by the fact, that they build spontaneously a stable monolayer on a suitable substrate, due to the high affinity of the head group to the substrate surface. Because of this specific effect, it is possible to use various coating methods and different solvents. Self-assembled monolayers have great potential in terms of biocompatibility, molecular recognition, control of adhesion and wetting and sensitizing for photon trapping.[62]

SAMs can be prepared by dipping the substrate in the solution with the corresponding molecules[63] (see Figure 9) or via spin coating (see Chapter 4.1.). Other methods are the gas phase deposition and the organic molecular beam epitaxy.[64]

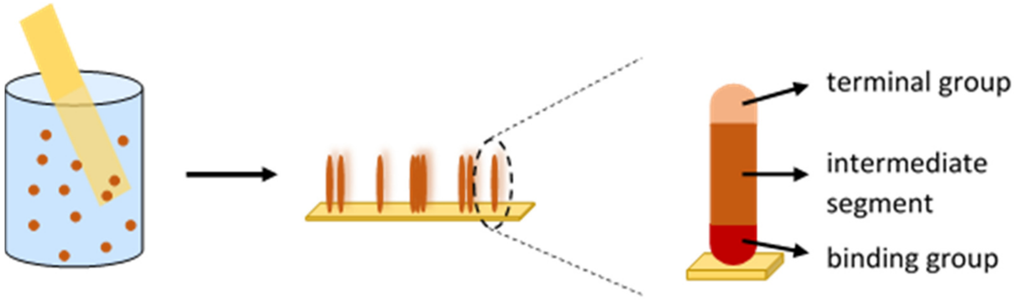

Figure 9: Immersing a substrate in a solution with SAMs (according to reference 63).

One theory for the formation of SAMs is according to Schwartz[62], that the molecules are transported through the solution via diffusion or convection. Then the chemisorption of the surface binding group on the substrate occurs. This adsorption processes stepwise. Individual molecules will be attached until a close-packed film, consisting of a two-dimensional molecular composition, is generated. The general structure (see Figure 9) of these molecules consists of the binding group adjusted to the substrate, a segment of an alkyl chain or aromatic rings and the terminal group, which is responsible for the properties of the surface. The adsorption occurs via one, two or more sites (see Figure 10) depending on the binding group.[62,63,64]

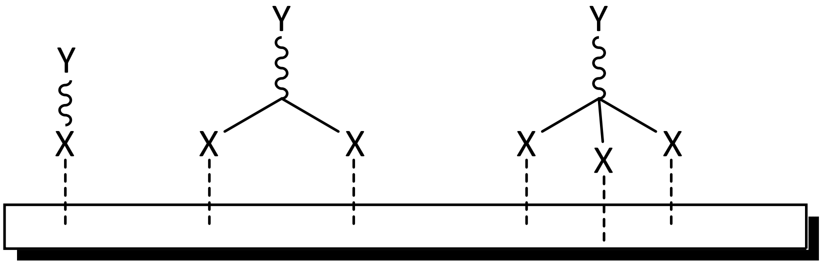

Figure 10: Adsorption on the substrate (according to reference 65).

One of the most studied molecule groups for the formation of monolayers are alkanethiols and dithiols, due to the great affinity of sulfur to metals.[45,46] Silanes and organic acids are very appropriate too, because of their ability to attach on oxides and native oxide layers.[47-61]

Due to the fact, that free charge carrier transport through devices depends on surface and interface qualities, the insertion of self-assembled monolayers is a good possibility to control as well as to improve these properties.[45-61]

2.3. Overview of SAMs in OPV

There are several possibilities, where you can insert self-assembled monolayers in a solar cell device, such as on the ITO coating or on various buffer layers.[45-61]

Generally, self-assembling molecules with an electron-withdrawing group (positive dipole moment) create a dipole moment, which has the same orientation as the built in electric field. This leads to an enhanced work function. Is the dipole aligned in the other direction, and the molecules have electron-donating groups (negative dipole moment), the WF is lowered (see Figure 11).[46-48,50-55,60,61] Moreover, the SAMs influence the morphology of the photoactive layer, resulting in an improved charge separation as well as in better charge transport features.[46-48,50-55,60,61,]

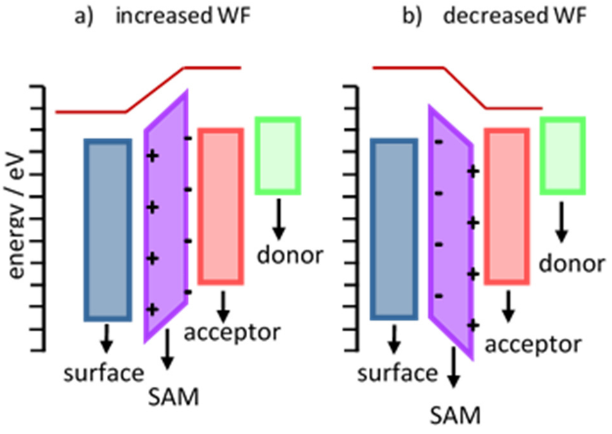

Figure 11: Influence of the dipole moment (according to references 46-48, 50-55, 60, 61).

2.3.1. SAMs on ITO

As mentioned above, indium tin oxide possesses several advantages as an electrode material. However, there are specific problems in the use of untreated ITO. One is the enhanced series resistance due to the low work function (4.7 eV),[48,66] another is the low wetting of the organic semiconductors because of its hydrophilicity.[46,47,49,52,55,61] In addition to the treatment with oxygen-plasma,[67] as well as with ozone[68] and coating with PEDOT:PSS[12,13,15,27-29,35,40,43] , there is also the possibility to apply a self-assembled monolayer.[45-61]

Khodabakhsh et al.[52] examined the influence on the work function of ITO in CuPc:C_{60} (CuPc: copper phthalocyanine) based solar cells through three molecules with a positive dipole moment– 4-chlorobenzoylchloride (CBC), 4-chlorobenzene-sulfonyl chloride (CBS) and 4-chlorophenyldichlorophosphate (CBP) –which differ only by their binding site (see Figure 12):

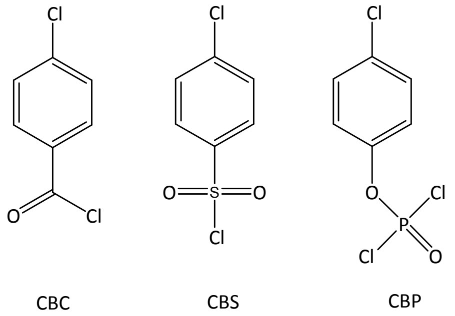

Figure 12: Structure of CBC, CBS and CBP (according to reference 52).

The short circuit current density, the fill factor and the power conversion efficiency increased, due to the better wettability of the photoactive layer and the adaption of the WF. The insertion of the chlorinated phenylene group caused a higher hydrophobicity and thus an improved wetting, which was confirmed by a significantly increased water contact angle. The enhanced I_{SC} and FF was closely related to the influence of the charge-transfer rate at the transparent electrode. This led to a lower series resistance and therefore to a better charge collection before recombination of the free charge carriers. Reason for this was the dipole moment towards the conducting electrode mentioned above. However, the SAMs had no effect on the open circuit voltage. According to S. Khodabakhsh, this was mainly because of the small difference of 0.3 eV between the various work functions and the HOMO level of the used donor molecule copper (II) phthalocyanine.

Interesting results emerged from the work of Jones et al.[61] concerning an increased V_{OC} due to an improved adjustment between the work function of the ITO electrode and the

HOMO level of the donor molecules CuPc, chloroaluminium phthalocyanine (ClAlPc) and boron subphthalocyanine (SubPc):

> Solar cells with CuPc delivered nearly the same results as S. Khodabakhsh published. However, with (ClAlPc) and (SubPc) the V_{OC} increased from 0.47 V to 0.80 V and from 0.56 V to 0.95 V. According to Jones et al. this was caused by the better adaptation of the energy levels ($\Delta = 0.3$ eV) and by a reduction of voids on the ITO surface. However, the better adhesion due to the more hydrophobic self-assembled monolayer was also mentioned.

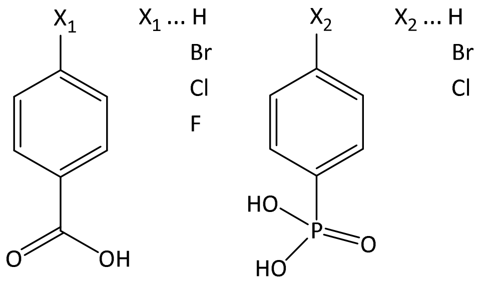

Figure 13: Structure of the used benzoic acids and phosphonic acids (according to reference 61).

> The molecules used (see Figure 13) – benzoic acid, phosphonic acid and three halogenated para-substituted derivates – increased the I_{SC} and FF. Here as well, a decreased resistance at the interface of the conducting electrode and the photoactive layer led to an improved charge collection.

H. Bedis[46] investigated the effect of alkanethiols and benzoic acid derivates (see Figure 14) on ITO substrates of α-sexithiophene based solar cells:

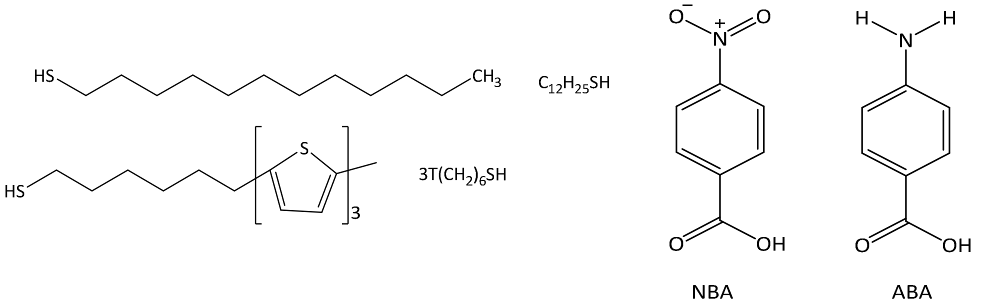

Figure 14: Structures of the thiols and BA derivates (according to reference 46).

Both alkanethiols had effects on the orientation of the molecules of the photoactive film, deposited on the SAM layer, which led to enhanced mobility of the free charge carriers. As a result, the I_{SC} as well as the V_{OC} were increased. However, there was no influence on the fill factor. The benzoic acid derivates used differed in their dipole moments. NBA had a very strong negative and ABA a positive one. As mentioned above, the work function and the efficiency were associated to the direction of the SAMs' dipole. The dipolar moment of NBA was contrary to the inner electric field, which led to a low V_{OC}. However, the I_{SC} was increased, which could be explained by the high dipole moment of -5.94 D and related to an efficient dissociation of excitons. Whereas, the orientation of the dipole moment of ABA was similar to the direction of the bulk-internal field. In solar cells with ABA as a self-assembled monolayer, the current density showed a significant increase, but also the V_{OC} rose slightly. H. Bedis clearly showed the influence of the alignment of the dipolar moment and the effect of a high dipole moment on the I_{SC}.

Macaraig et al.[55] used SAMs with different binding sites, various dipolar moments as well as aromatic groups – 1-pyrenecarboxylic acid, 2-naphthaic acid, benzoic acid and 4(-thiophen-2-yl) benzoic acid (see Figure 15) to improve P3HT:PCBM based solar cells:

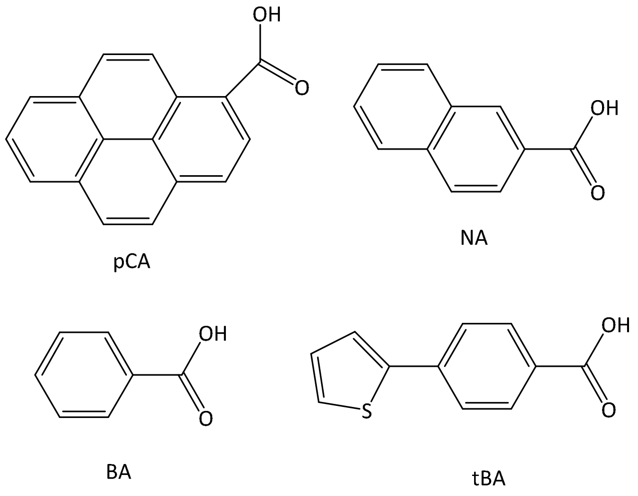

Figure 15: Structures of molecules used (according to reference 55).

The number and the type of the aromatic groups had effects on the I_{SC} with respect to recombination of the free charge carriers and the possible absorption of electrons from the acceptor material. This led to the formation of a reverse current, and thus to

> a reduction of the I_{SC}. Solar cells with pCA provided the lowest photocurrent density. The best values were achieved with BA as a monolayer. The I_{SC} from tBA-modified devices was increased, as compared to the NA-modified. Reason for this was the fact, that the thiophene group was further away from the ITO surface than the naphthyl group. In contrast to the working groups mentioned above, Macaraig et al. assumed that the dipole moment change the V_{OC} instead of the I_{SC}. A dipole moment towards ITO led to an enhanced V_{OC}, whereas an oppositely directed dipole decreased the open circuit voltage.

2.3.2. SAMs on Buffer Layers

Buffer layers for enhanced electron transport, should consist of a large-bandgap semiconductor with a conduction band edge lower than the LUMO of the acceptor material.[54] Additionally ETLs should have a high electron mobility. Well-known examples of such films are TiO_X and zinc oxide (ZnO).[30-32,47,53,54,60,69] As mentioned above, within inverted solar cells, the electron transport layer is placed between the transparent electrode and the photoactive material. In normal devices, there is the possibility to insert an ETL between the active layer and the metal contact.

Jen et al.[54] worked on the modification of ZnO via SAMs for a better adaptation to metals used for electrodes:

> Unlike to SAMs in contact with the polymer:acceptor blend, the effective dipole moment of self-assembling molecules changed, when they were applied on a buffer layer prior to the metal contact (see Figure 16).

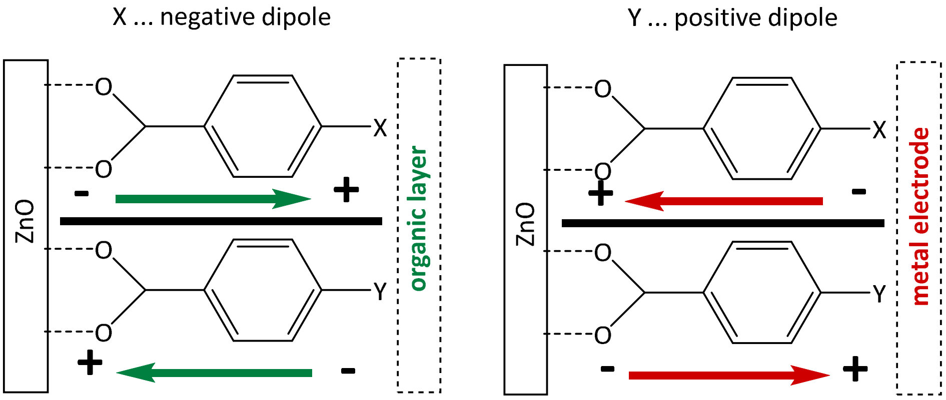

Figure 16: Differences in the net dipolar moment (according to reference 54).

In this case, a dipole moment was needed that was directed away from the metal electrode. This led to a better tuning of the conductive band of ZnO with the work function of the metal used. An opposite dipole increased the Schottky barrier, thus the Ohmic contact was worsened and as a result, the V_{OC} was reduced. Devices with SAMs having a negative dipole moment showed enhanced values of I_{SC} and V_{OC} as well as a decreased series resistance. By applying SAMs with a net dipole in the right direction, metals with a high work function such as silver or gold could be used.

Kim et al.[60] investigated the influence of three para-substituted benzoic acid derivates (see Figure 17) on the effective work function of ZnO in inverted P3HT:PCBM solar cells:

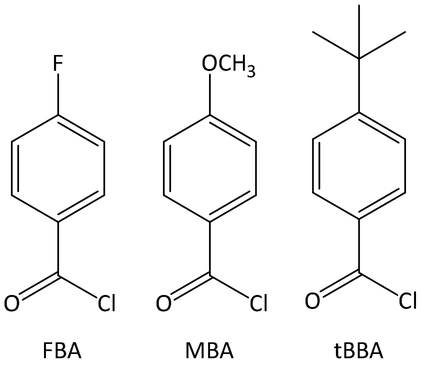

Figure 17: Structures of 4-fluoro-, 4-methoxy- and 4-tert-butyl benzoic acid (according to reference 60).

The dipole of the FBA monolayer was directed towards the ZnO surface, leading to an increase of the effective work function. This resulted in a lowering of the V_{OC} values. SAMs with a dipole in the opposite direction decreased the WF of ZnO, resulting in a slightly enhanced voltage. However, significant differences occurred in the current density. Here, the substituents affected the morphology of the photoactive film. This assumption was confirmed by transmission electron microscopy (TEM) and atomic force microscopy (AFM) measurements. In FBA treated devices PCBM formed large domains (80 – 130 nm), however, in cells with tBBA, these areas were smaller (30 – 40 nm). The best aggregate size was formed with MBA as a monolayer. Their dimension was exactly in the range of the exciton recombination length. Furthermore, the roughness of the active layer on ZnO:FBA was much higher than for the other device compositions. By comparing these data with the I_{SC} and FF, a linear correlation was shown. The higher the current density and the fill factor was, the smaller the PCBM domains and the more flat was the surface of the active layer. Kim et al. showed that both the orientation of the effective dipolar moment as well as the terminal group – with respect to the hydrophobic character - of the self-assembling molecules used were important parameter for an efficient organic solar cell.

The working group of W. Choi and K. Cho[47] focused their study on the control of the surface energy by coating a ZnO surface with mixed SAMs consisting of two silanes with different terminal groups and intermediate segments:

In order to ensure a certain degree of hydrophilicity, an aminopropyltrimethoxysilane was used in combination with octyltrimethoxysilane for the control of the hydrophobic properties (see Figure 18).

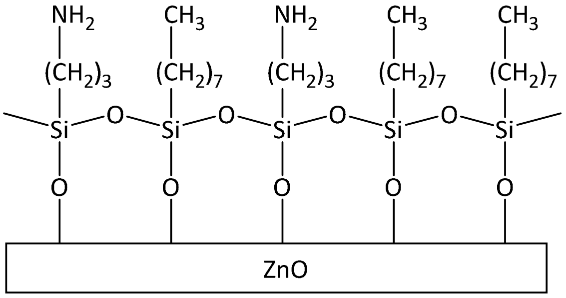

Figure 18: Mixed SAM on ZnO (according to reference 47).

By variation of the percentage of alkylsilane, the surface energy was reduced from 70 mN/m at 0 % to 25 mN/m at 80 % content, respectively. Since both molecules had an electron-donating group, the WF of ZnO remained the same. Therefore, the change in current density was due to the modification in the surface tension. The highest values of I_{SC} could be found at energies in the medium range, which was slightly located above the neutral zone (area between the surface energies of the donor and the acceptor). Here, vertical phase separation occurs predominantly distinguished by a uniform morphology. Furthermore, the lower the surface tension the higher is the probability of non-wetting. Thus, there is a defined area of surface energy needed to ensure the best possible interpenetrating network of the donor and acceptor for improved charge generation and transport. There is no effect on the V_{OC}, because the work function of the ZnO layer does not change.

An interesting approach delivered the work of Jen et al.[70] regarding the SAMs used in heterojunction (which is built with P3HT and the fullerene modified SAMs) as well as in bulk heterojunction (P3HT:PCBM with further fullerene modified SAMs) solar cells:

A C_{60}-fullerene was modified with benzoic acid (SAM1 and SAM5), with catechol (SAM2) and with phenylphosphonic acid (SAM3). Additionally a PCBM modified with benzoic acid (SAM4) was used (see Figure 19).

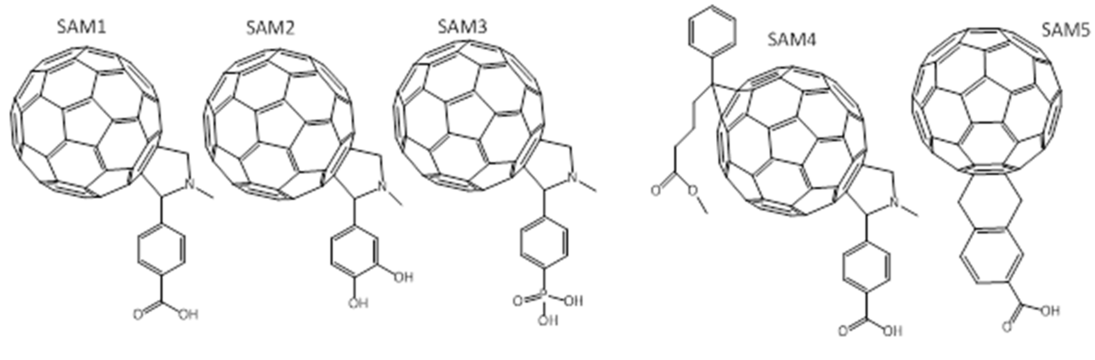

Figure 19: Structure of the C_{60} modified molecules used (according to reference 70).

Since the formation of the monolayer depended on the affinity of the binding sites, two different coating methods were carried out. First, the SAMs were applied via spin coating. Contact angle measurements were performed to ensure the existence of the monolayer. Due to the fact, that the time to react with the surface was very short using this method and some contact angle values were low, a second method was used. Therefore, the ZnO substrates were dipped in a solution of the SAMs for a defined time. Interestingly, only SAM2 showed a higher contact angle with the second method, suggesting that the catechol group needed more time to adsorb at the ZnO surface than the benzoic acid. The contact angle of SAM3 decreased significantly after ten minutes, which showed that ZnO was attacked by the phosphonic acid. All SAM-modified P3HT heterojunction devices showed a lower V_{OC}, the values for I_{SC}, FF und PCE, however, were increased. The lower voltage could be explained with the dipole moment between the ZnO and the carboxylic and catechol group. The influence of the acidic nature of the phosphonic group was also seen in the performance of the solar cells. After 240 minutes dipping in the SAM3-solution, the solar cell showed no behavior as a photodiode anymore. Due to the good ability of the fullerene to accept electrons, the photocurrent density was increased. Hardly any difference could be seen in P3HT:PCBM BHJ solar cells. There was only an I_{SC} enhancement of about 5 % because of the better charge transport through the self-assembled monolayer to the ETL.

Another material that is often used for an electron transport layer is TiO_X. The work functions of titanium oxide are 4.4 eV and 7.6 eV, respectively.[71] Here again, the coating with a self-assembling monolayer leads to an enhanced performance due to a better tuning of the oxide film with the photoactive material, the reduced charge recombination and the positive effects on the morphology.[72]

McGehee et al.[53] investigated the influence of three different groups of SAMs between a TiO_X and a P3HT layer; for simplification, no acceptor was used:

The first molecules applied were para-substituted benzoic acid derivates (terminal groups: $-SO_2F$, $-NO_2$, -CN, -Br, -H, $-OCH_3$ and $-NH_2$). If the dipole moment by the use of electron-withdrawing substituents is directed to the TiO_X layer, there was a reduction of the gap between the energy level of the oxide and the HOMO of the polymer. This led to significantly smaller values of V_{OC} (Δ= 0.2 V). However, when coating the ETL with electron-donating molecules, leading to a larger offset of energy levels, the effect on the voltage was lower ($\Delta \approx 0.05$ V). A better tuning of the energy levels of TiO_X and polymer led to a higher concentration of electrons and holes. Consequently, the free charge carrier recombination was accelerated and the turn-on of the dark current was leading sooner to a low V_{OC}. The influence of the SAMs on the I_{SC} was exactly the opposite. Molecules with electron-withdrawing groups increased the short-circuit current and those, with electron-donating groups decreased it.

The next molecules used were benzene carboxylic acids with a different number of carboxylic groups (see Figure 20):

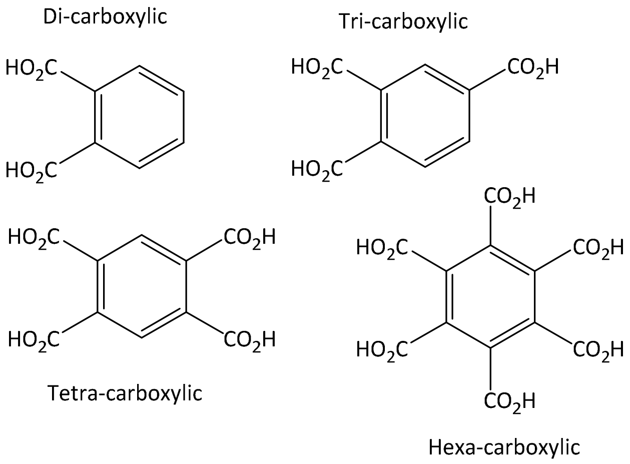

Figure 20: Structure of the benzene carboxylic acids used (according to reference 53).

These self-assembling molecules influenced the work function of the ETL through protonation of the TiO_X via acid-base reactions. The more acid groups existed the lower was the V_{OC}. This could be explained by the enhanced protonation of the oxide surface. Interestingly, there were slightly changes in voltage by the use of self-assembling molecules with more than four substituents, because of the probably lower number of available binding sites on the TiO_X film. However, the number of carboxyl groups had a large impact on the I_{SC} due to the electron affinity.

Ruthenium(II) dyes formed the third molecule block. They allowed a fast electron transport from the polymer to the TiO_X and additionally they had internal dipole moments from the asymmetry of the HOMO and LUMO level. In addition, here the protonation of the ETL led to a lower voltage. All three molecules increased the I_{SC}, which could be explained by the higher exciton dissociation of the coated TiO_X.

In summary, SAMs on an ITO surface or on a buffer layer have different impacts on the solar cell characteristics:

- Increased I_{SC}, FF and PCE values are obtained due to the better wettability of the oxide surfaces and the better adaption of the work function.[46,47,52,61]
- Enhanced I_{SC} and FF are related to a lower series resistance because of better charge collection before recombination.[46,52-55,61]
- A better adaption of the energy levels of ITO or the buffer layer and photoactive layer as well as a reduction of voids on the surface lead to higher V_{OC} values.[46,55]
- SAMs have effects on the orientation of the donor and acceptor molecules, which increases the I_{SC} as well as the V_{OC}.[46]
- A higher recombination rate leads to a lower V_{OC}.[53]
- A dipole moment towards the oxide surfaces increases the I_{SC} and the V_{OC}.[46,52-55,61]
- SAMs influence the morphology of the active layer: the smaller the domains of PCBM and P3HT are, the higher are the I_{SC} and FF.[60]

2.4. Aim of this thesis

This work investigates the influence of self-assembling monolayers, deposited onto charge carrier selective transport layers, on the performance of bulk heterojunction solar cells. For this, organic molecules with an intrinsic dipole moment are used, which has various effects on the efficiency of the organic photovoltaic cells, for example:

- Improved contact between the buffer layer and the active organic layer.[46,47,52,61]
- Controlling of the electronic properties such as work function (WF) and electron affinity.[46,47,52-55,61,70]
- Reduction of series resistance (R_S).[54]
- Increasing the wettability.[46,47,52,61]

The first part this work focuses on the modification of a vanadium oxide (V_2O_5) film, as a hole transport layer (HTL) in a normal OPV architecture and in the second the modification of a titanium oxide (TiO_X) as an electron transport layer (ETL) in inverted polymer solar cells. For this purpose, benzoic acid, four different para-substituted derivates thereof and two phosphonic acids are used. Several coating strategies, as well as different solvents for the SAMs are tested. For investigation of the monolayer, water contact angle analysis and X-ray photoelectron spectroscopy (XPS) measurements are performed. In addition, the series resistance of the cells is calculated and the solar cells are characterized with current-voltage measurements in the dark and under illumination.

3. RESULTS AND DISCUSSION

First, the influence of five different molecules, which are able to form a self-assembling monolayer, on V_2O_5 as a hole transport layer and TiO_X as an electron transport layer with respect to the wetting properties is investigated. For this purpose, benzoic acid (BA) and four different para-substituted derivates thereof, 4-fluorobenzoic acid (FBA), 4-methoxybenzoic acid (MBA), 4-cyanobenzoic acid (CBA) and 4-*tert*-butylbenzoic acid (tBBA), are used (see Figure 21).

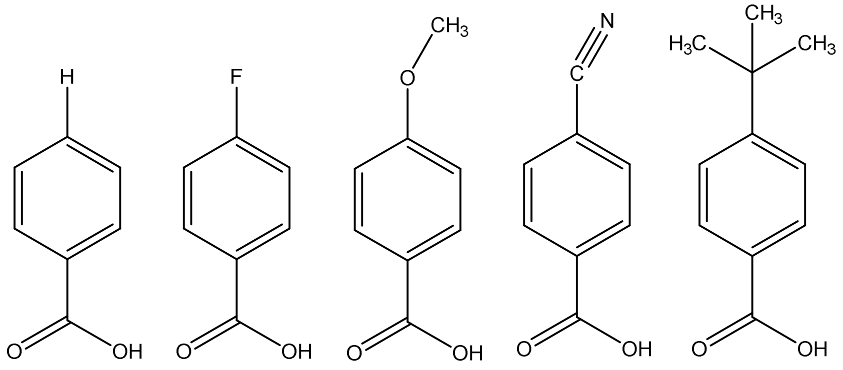

BA FBA MBA CBA tBBA

Figure 21: Self-assembling molecules used on V_2O_5 and TiO_X.

To investigate the coating of the SAMs on the oxide layers, water contact angle measurements as well as XPS measurements are performed.

3.1. Contact Angle Measurements

Contact angle measurements provide a statement about the wetting properties of a surface. The lower the contact angle is, the better is the wettability. Contact angles are formed at the interface solid/ liquid/ gaseous resulting in three surface tensions (see Figure 22).[73]

The Young-equation describes the relation between these surface energies: [73]

- Of the solid $\sigma_{s,g}$ $_{s}$ … solid, $_{g}$ … gaseous
- Of the liquid $\sigma_{l,g}$ $_{l}$ … liquid
- Of the interface solid/ liquid $\sigma_{s,l}$

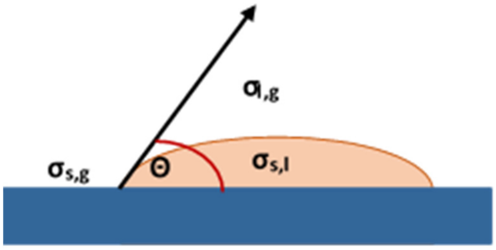

$$\cos\theta = \frac{\sigma\,(s,g) - \sigma\,(s,l)}{\sigma\,(l,g)}$$

Figure 22: Contact angle, surface tensions and Young-equation (according to reference 73).

For verification of the SAM-coating, the sessile drop method, also called method of the static contact angle is used. For this purpose, the contact area between the solid and the liquid does not change realized by immediate photograph of the sessile drop.

The formation of the SAMs on the oxide surface leads to a change in the surface energy and thus, a significant change in the contact angle. Due to the apolar character of the end groups of the molecules used, a higher contact angle of water is expected. In the case of measurements with water, a high contact angle is preferred as P3HT:PCBM is an apolar system. Different SAM preparation methods were tested leading to different contact angles of water, which indicated a denser monolayer using approach #2.

3.1.1. SAMs onto V_2O_5

For the preparation of the V_2O_5 layer, a precursor solution of vanadium(V)oxytriisopropoxid in isopropanol is applied via spin coating on the cleaned and activated ITO surface. To obtain a V_2O_5 network, the coated substrates are stored at air for at least one hour (according to a method of N. Özer[74]). The reaction is shown in Figure 23.

$$(C_3H_7O)_2OV(OC_3H_7) + H_2O \longrightarrow (C_3H_7O)_2OV(OH) + C_3H_7OH$$

$$(C_3H_7O)_2OV(OH) + (C_3H_7O)_2OV(OC_3H_7) \longrightarrow =(OV\text{-}O\text{-}VO)= + C_3H_7OH$$

Figure 23: Hydrolysis of vanadium(V)oxytriisopropoxid (according to reference 74).

After the treatment of the V_2O_5 layer in the plasma etch chamber, the self-assembling molecules are applied via different routes. In order to compare the results of the SAM-coated devices, substrates only with V_2O_5 as a buffer layer are made.

First, a method of Kim et al.[60] has been adopted, by spin coating a 1.0 mg/ml solution of the self-assembling molecules. To remove the not tightly bound molecules, the substrates are rinsed with 10 ml pure acetone.

The changes of the water contact angle are summarized in Table 1.

Table 1: Water contact angle of pure V_2O_5, rinsed with acetone and coated with SAMs.

	Θ H_2O/ °	**±**		**Θ H_2O/ °**	**±**
V_2O_5	16.5	2.7	*tBBA*	68.6	5.5
Acetone	35.2	2.9	*BA*	72.4	5.1
CBA	63.3	2.7	*MBA*	72.3	2.3
FBA	68.6	1.7			

Based on the change of the contact angles from very hydrophilic to more hydrophobic values, one can assume that the coating with all five self-assembling molecules was successfully. The found contact angles between 68°-72° are similar for all molecules except CBA, with a significant lower value of 63° because of the more polar cyano end group.

In the second approach, the washing procedure is changed. The molecules not chemically adsorbed are removed by spin coating with pure acetone. The results of the contact angle measurements are summarized in Table 2.

Table 2: Water contact angle of pure V_2O_5, rinsed with acetone and coated with SAMs.

	Θ H_2O/ °	±		**Θ H_2O/ °**	±
V_2O_5	16.5	2.7	tBBA	67.3	1.2
Acetone	40.4	1.8	BA	72.5	2.6
CBA	64.5	0.8	MBA	71.1	1.2
FBA	68.3	2.1			

Using the second approach, the contact angles are in the range of the first method, but here the variation is much smaller (see Figure 24). Based on these results, the second method is preferable, because of a better reproducibility. The measured values indicate that the type of removal influences the arrangement of the molecules.

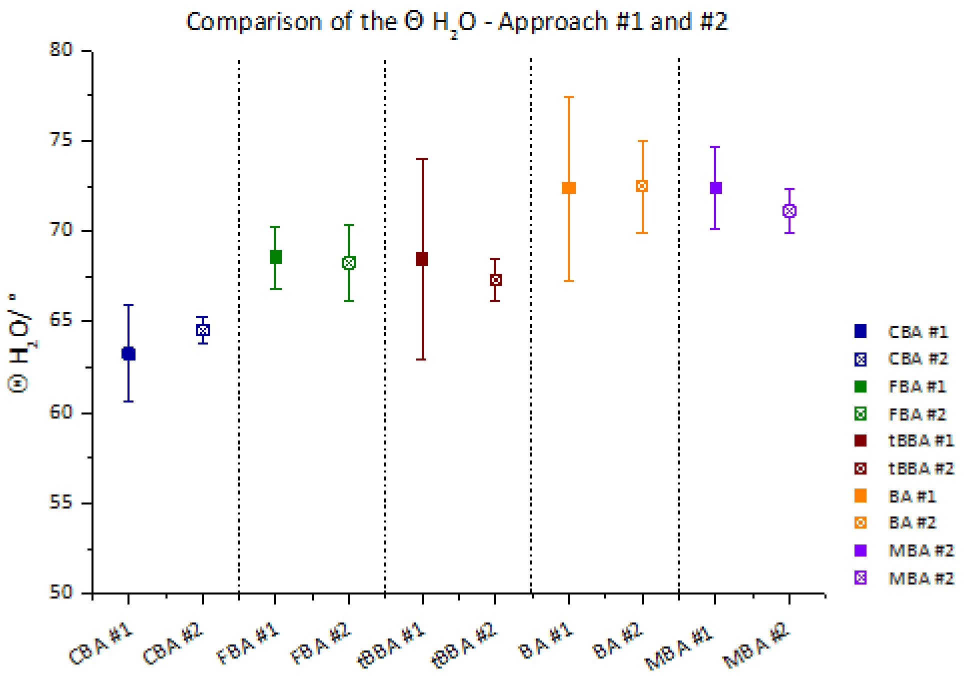

Figure 24: Comparison of the water contact angles of approach #1 and #2.

The comparison of these data with the results of the XPS measurements (see Chapter 3.2.), shows, that it is not easy to make precise statements about the coating of V_2O_5 with SAMs. According to the measured data, there is no uniform coating of the oxide surface with the SAMs.

In a third approach, tetrahydrofuran (THF) as a further solvent is used. Therefore, approach #2 is applied. Table 3 shows the measured contact angles of the SAM treated V_2O_5 surface with THF.

Table 3: Water contact angles – THF as solvent.

	Θ H_2O/ °	±		***Θ H_2O/ °***	±
V_2O_5	16.5	2.7	tBBA	73.5	0.9
THF	31.9	0.5	BA	86.3	0.7
CBA	80.8	1.1	MBA	86.1	0.5
FBA	82.1	2.0			

The contact angles are increased by approximately 15°, an exception is tBBA dissolved in THF with only a slight increase of 5° (see Figure 25). This suggests an influence of the solvent used. The order of the self-assembling molecules could be affected.

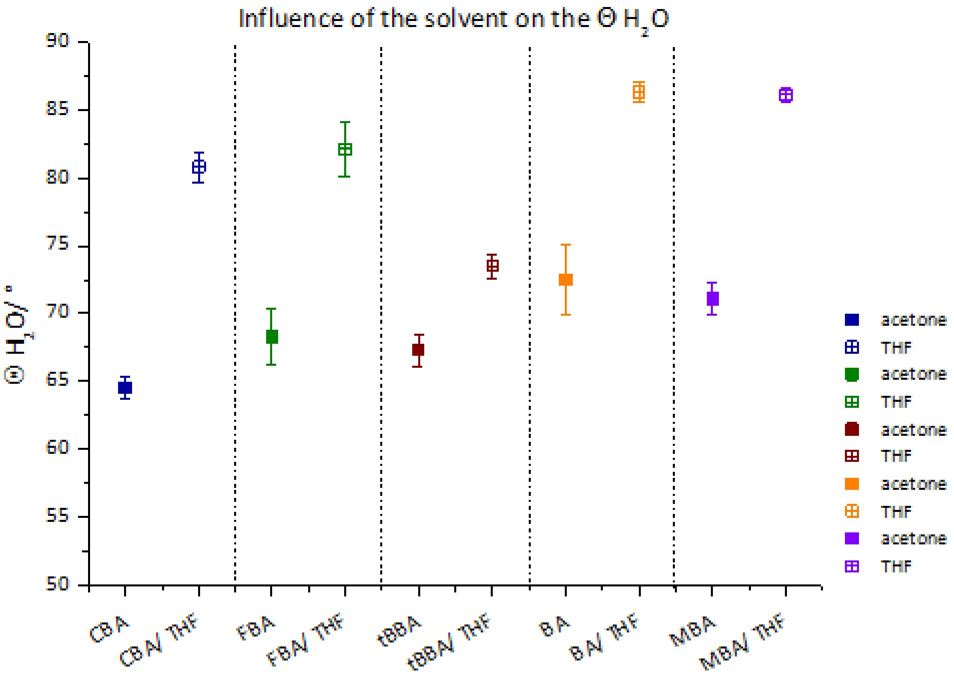

Figure 25: Influence of the solvent on the water contact angle.

3.1.2. SAMs onto TiO_X

The formation of the TiO_X layers is carried out via the following two methods:

- A titanium diisopropoxide bis (acetylacetonate) precursor solution is applied via spin coater on the cleaned and activated ITO surface followed by annealing at 400°C for conversion into the TiO_X layer.
- Vapor deposition of metallic titanium using a vacuum deposition system under ambient conditions.

For the preparation of SAMs on TiO_X layers, the same approaches (#1 and #2) as described before, are used.

Table 4 show the changes in the water contact angles.

Table 4: Measured water contact angles of TiO_X coated with SAMs.

Approach #1					
	Θ H_2O/ °	**±**		**Θ H_2O/ °**	**±**
TiO_X	16.6	1.2	tBBA	64.5	4.4
MeOH	36.3	0.9	BA	75.9	8.6
CBA	71.9	2.5	MBA	60.6	4.3
FBA	78.8	8.4			
Approach #2					
	Θ H_2O/ °	**±**		**Θ H_2O/ °**	**±**
TiO_X	16.6	1.2	tBBA	56.0	2.2
MeOH	36.3	0.9	BA	55.8	2.3
CBA	54.2	2.2	MBA	56.6	6.8
FBA	64.4	2.1			

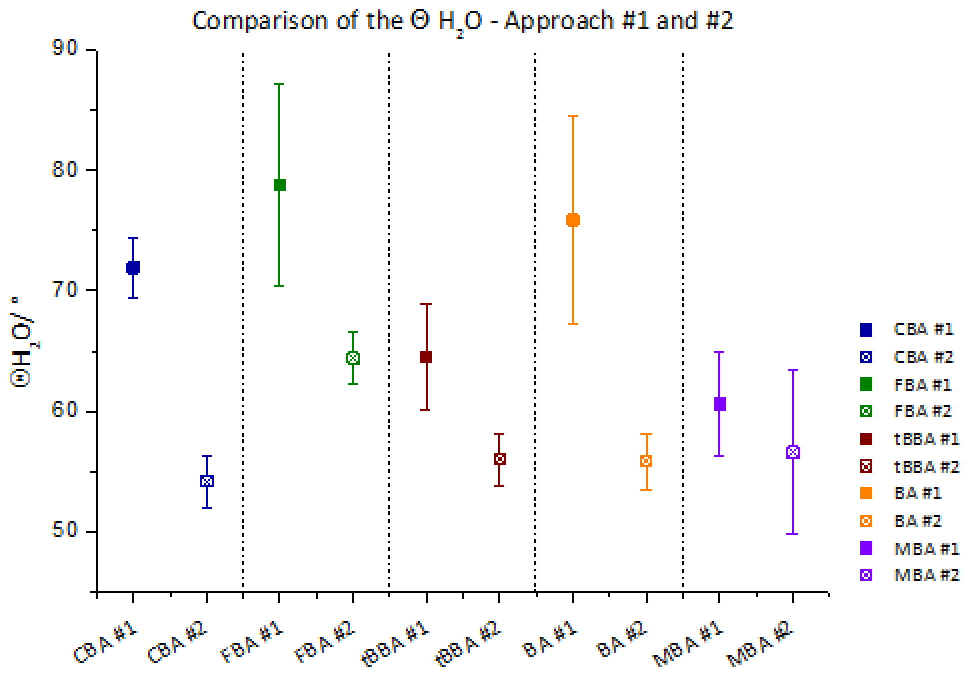

Figure 26: Comparison of the water contact angle – approach #1 and #2.

It is seen, that the contact angles of approach #2 are not as high as in the first approach (see Figure 26). The type of removal has a significant influence on the wettability of water. Here also, using the second approach, the standard variance is smaller, except TiO_X coated with MBA. The overall lower values in approach #2 cannot be explained.

Next, a vapor-deposited TiO_X is used as an ETL. Approach #2 is used for coating the TiO_X surface. It is noticeable, that the evaporated TiO_X already has a higher contact angle than the solution-processed. Further, be assumed here that due to the small standard variance a uniform surface is present. tBBA has the highest value, which matches the hydrophobic nature of the *tert*-butyl group. Why this is only here the case, is unclear. Figure 27 shows the measured water contact angles.

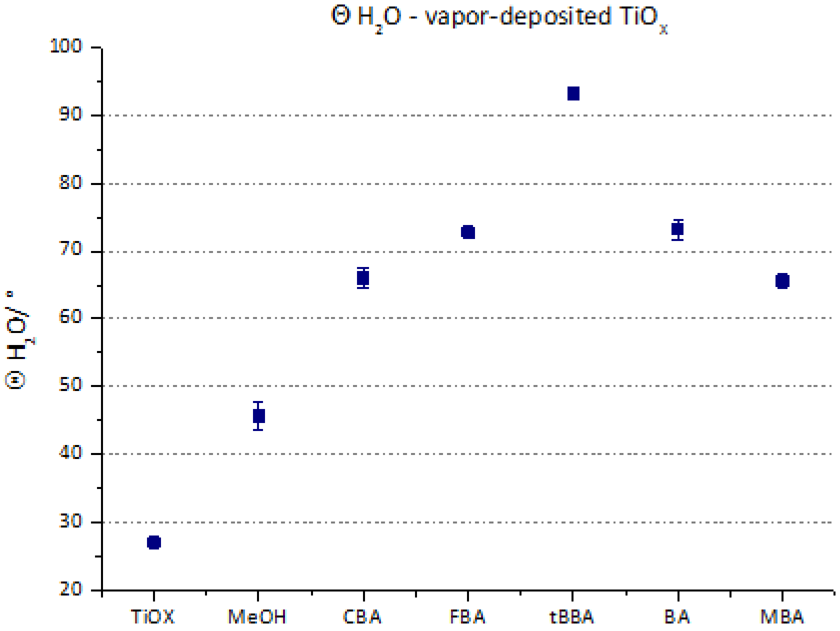

Figure 27: Water contact angles – vapor-deposited TiO_X.

3.2. XPS Measurements

X-ray photoelectron spectroscopy is used as a surface characterization method for nondestructive analysis of the element composition. By irradiation with X-rays (typical energy: 1486.6 eV), the top nanometers of the sample can be examined.

Thereby, each element to be investigated provides a characteristic signal. This peak corresponds to the electron configuration of the electrons in the respective atom. The number of detected electrons corresponds to the respective element content in the sample.[75]

The coating of the SAMs is carried out via spin coater (see Chapter 4.2.). Two spots are investigated per sample. The following part shows relevant XPS data. The entire data can be found in the Appendix.

- V_2O_5

V_2O_5 is used as the hole transport layer in the normal device architecture, and therefore the coating of it with the SAMs – CBA, FBA, tBBA, BA and MBA – as well as the pure V_2O_5 surface is examined.

The measured binding energies correspond to the literature values, 530.4 eV for O 1s and 524.0-517.8 eV for V 2p3.[74] Based on the ideal composition of V_2O_5 (stoichiometry O/V is 2.5), an element distribution of 3.1 (stoichiometry O/V) is obtained from the measured data. A possible explanation is an adsorption of water on the surface. Furthermore, impurities of carbon and nitrogen are found on the surface. These originate from the exposure of the sample to air.

Table 5 shows the measured data of the V_2O_5 surface. The corresponding spectrum is shown in Figure 28.

Table 5: XPS data of V_2O_5.

	Spot 1		Spot 2	
	Atomic/ %	**Peak Binding Energy/ eV**	**Atomic/ %**	**Peak Binding Energy/ eV**
C1s	20.68	284.30	20.93	284.32
O1s	59.22	530.27	58.15	530.29
N1s	1.51	401.78	2.24	401.15
V2p3	18.59	517.11	18.69	517.10

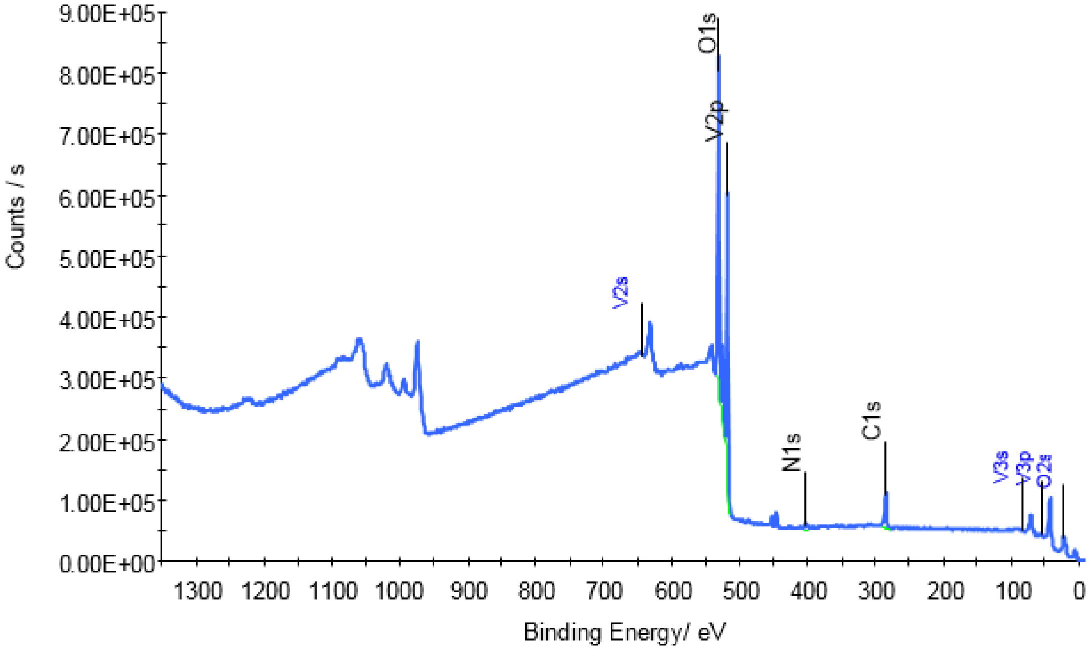

Figure 28: Survey scan of V_2O_5, Spot 1.

- TiO_X

TiO_X is used as an electron transport layer in the inverted device architecture. Substrates with benzoic acid as well as with the derivates thereof and additionally two phosphonic acid coated substrates are analyzed. The coating of the SAMs is the same as above. Here also, two spots per sample are investigated.

According to literature,[76] the binding energy of Ti 2p3 from titanium dioxide is around 459 eV. This value corresponds very well to the measured peak binding energy of the TiO_X sample (see Table 6). According to this, the ETL layer only consist of TiO_2. The corresponding survey scan is shown in Figure 29.

Table 6: XPS data of TiO_x.

	Spot 1		*Spot 2*	
	Atomic %	**Peak Binding Energy/ eV**	**Atomic %**	**Peak Binding Energy/ eV**
C1s	20.70	285.08	22.30	284.98
O1s	56.70	530.28	56.20	530.22
N1s	0.50	400.38	0.80	400.36
Ti2p3	20.90	458.81	20.70	458.36
Si2p	1.20	102.43	0.00	-

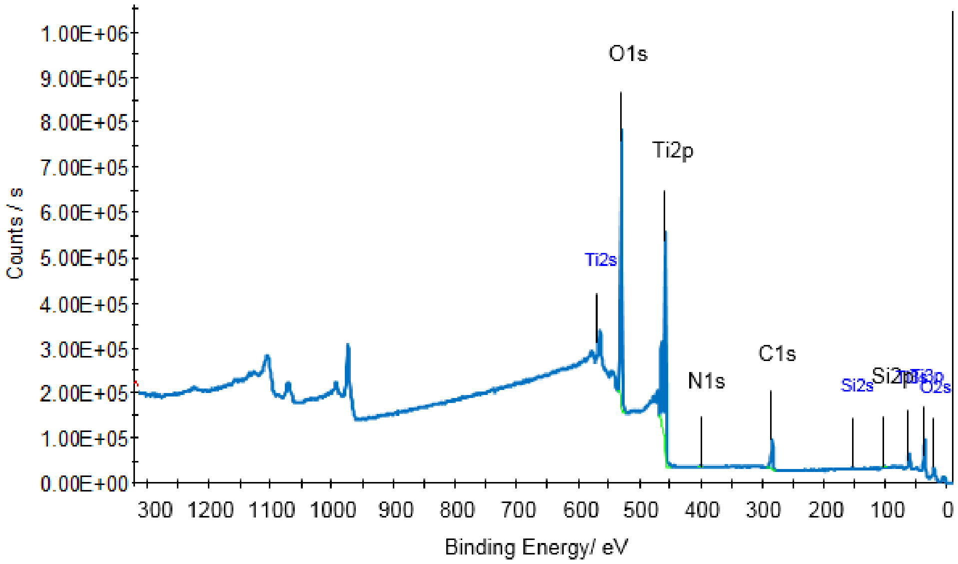

Figure 29: Survey Scan of TiO_x, Spot 1.

The stoichiometric O/Ti ratio is 2.0; however, the measured data provide an O/Ti ratio of 2.7. Therefore, it can be assumed that besides carbon, nitrogen and silicon contaminations, water is present on the surface.

- Benzoic acid

The XPS spectra of BA coated V_2O_5 and TiO_X show 3 carbon and 2 oxygen signals (see Table 7 and Figure 30 for V_2O_5 and Table 8 for TiO_X). Based on the literature,[77,78] the signals are assigned as follows:

- C1s Scan A: C-C/C-H from the aromatic structure (≈284 eV)
- C1s Scan C: π-π* satellite from aromatic structure (≈285 eV)
- C1s Scan B: C from the carboxylic group (≈288 eV)

- O1s Scan A: O from V_2O_5 or TiO_2 (530 eV)
- O1s Scan B: O from carboxylic group (531 eV)

Table 7: XPS data of V_2O_5 coated with BA.

	Spot 1		*Spot 2*	
	Atomic %	**Peak Binding Energy/ eV**	**Atomic %**	**Peak Binding Energy/ eV**
C1s Scan A	16.83	284.21	17.31	284.20
C1s Scan B	2.07	288.63	1.99	288.67
C1s Scan C	4.82	285.55	4.75	285.72
O1s Scan A	38.03	530.26	37.09	530.21
O1s Scan B	15.01	531.03	15.87	530.97
N1s Scan A	1.94	400.94	1.69	401.25
N1s Scan B	0.19	401.87	-	-
V2p3 Scan A	21.11	517.36	21.30	517.32

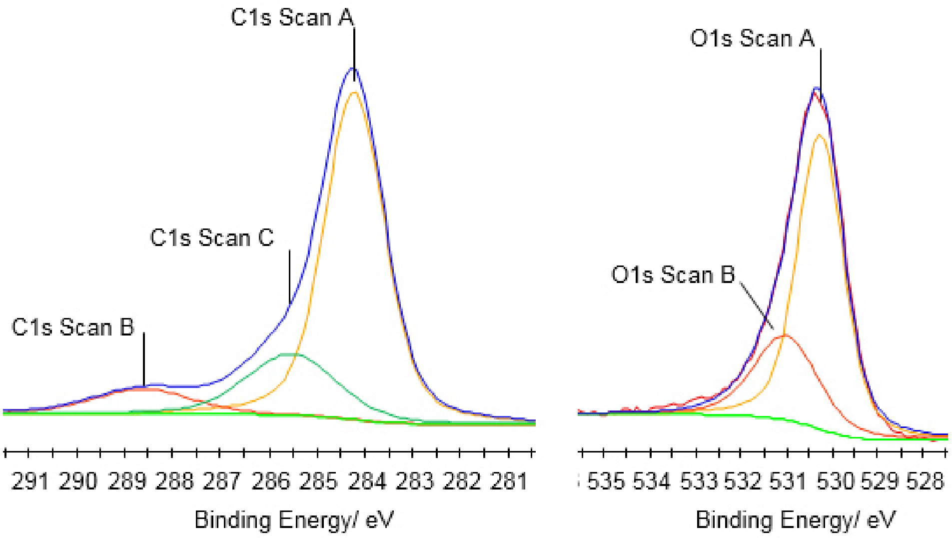

Figure 30: C1s Scan (left) and O1s Scan (right) of BA coated V_2O_5, Spot 1.

The ratio of the C1s Scan A and C1s Scan B signal (spot 1 and 2) of BA coated V_2O_5 should be 6:1. In fact, it is 8:1, which indicates, that impurities probably increases the C1s Scan A signal (such as carbon on the V_2O_5 surface). Another contamination is nitrogen.

The XPS data of BA coated TiO_x are shown in Table 8.

Table 8: XPS data of TiO_X coated with BA.

	Spot 1		*Spot 2*	
	Atomic %	**Peak Binding Energy/ eV**	**Atomic %**	**Peak Binding Energy/ eV**
C1s Scan A	9.60	285.02	21.09	284.46
C1s Scan B	2.57	289.17	2.23	288.40
C1s Scan C	18.05	285.85	3.39	285.67
O1s Scan A	38.43	530.48	41.17	529.72
O1s Scan B	11.41	531.88	10.63	531.09
N1s Scan A	0.20	400.28	0.88	400.59
N1s Scan B	0.85	401.07	0.34	399.16
Ti2p3 Scan A	18.89	459.02	20.26	458.24

Figure 31 shows the scan of C1s of the measured spots. At spot 1 can be seen, that the Scan A peak is much smaller than at spot 2. This disparity is may be due to a non-uniform coverage with BA or due to impurities.

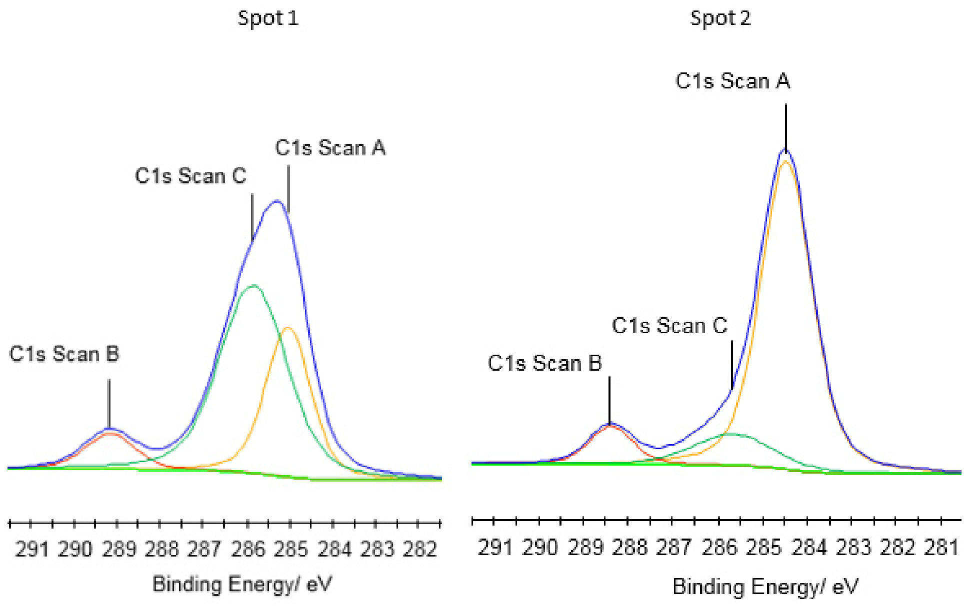

Figure 31: C1s Scan of BA coated TiO_X.

- 4-Fluoro benzoic acid

The XPS spectrum of FBA coated V_2O_5 shows no fluorine signal (see Table 9). Although the C1s and O1s signals go well with the literature values of pure benzoic acid (see Figure 32), must be assumed, that FBA at the two measured spots is not present. Possibly, only a very small amount of FBA adheres to the V_2O_5 surface. This assumption corresponds to the contact angle measurements (see Chapter 3.1.).

Table 9: XPS data of V_2O_5 coated with FBA.

	Spot 1		*Spot 2*	
	Atomic/ %	**Peak Binding Energy/ eV**	**Atomic/ %**	**Peak Binding Energy/ eV**
C1s Scan A	14.36	284.54	14.30	284.29
C1s Scan B	2.73	288.95	2.52	288.07
C1s Scan C	4.62	285.91	9.40	285.35
O1s Scan A	38.32	530.55	38.59	530.30
O1s Scan B	18.11	531.24	12.94	531.16
N1s Scan A	1.54	401.05	1.87	400.97
N1s Scan B	0.43	402.30	0.12	401.70
V2p3	19.89	517.74	20.26	517.39
F1s Scan A	-	-	-	-

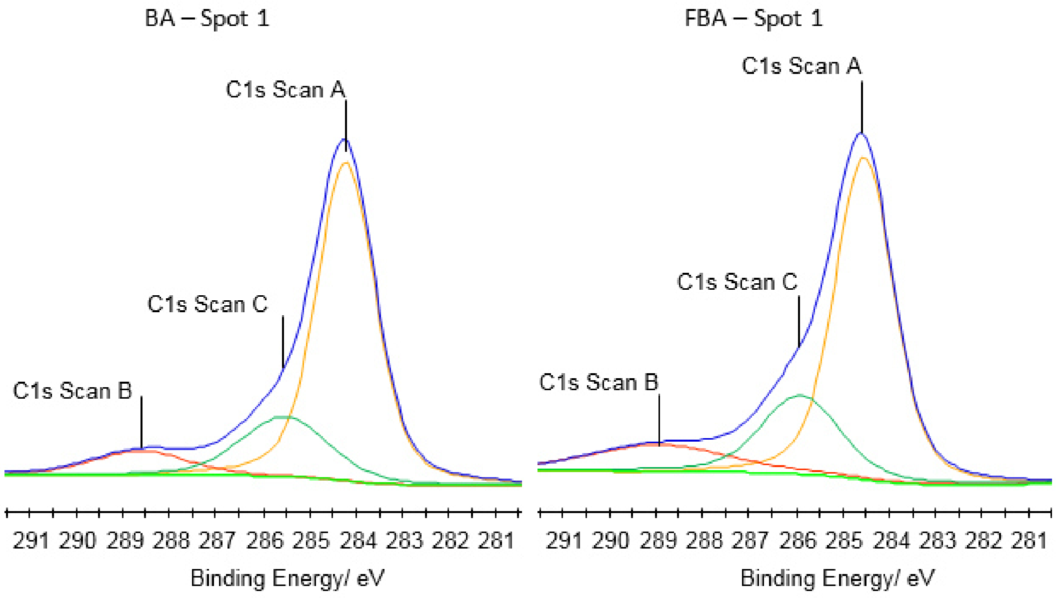

Figure 32: Comparison C1s Scan – BA and FBA coated V_2O_5.

Wherein the FBA coated TiO_X substrate, however, the fluorine signal is present (see Table 10).

Table 10: XPS data of TiO

	Spot 1		*Spot 2*	
	Atomic %	**Peak Binding Energy/ eV**	**Atomic %**	**Peak Binding Energy/ eV**
C1s Scan A	20.91	284.82	24.10	284.55
C1s Scan B	2.24	288.71	3.05	288.38
C1s Scan C	3.91	285.92	3.53	286.01
O1s Scan A	39.73	530.07	35.07	529.77
O1s Scan B	11.28	531.36	13.47	531.06
N1s Scan A	0.76	400.12	0.31	399.66
N1s Scan B	0.12	402.21	0.91	400.48
Ti2p3 Scan A	20.09	458.63	18.60	458.35
F1s Scan A	0.97	687.43	0.95	687.21

The C1s signals are similar to those of non-substituted benzoic acid (see Figure 33). Therefore, one can say, that the coating of TiO_X with FBA was successful.

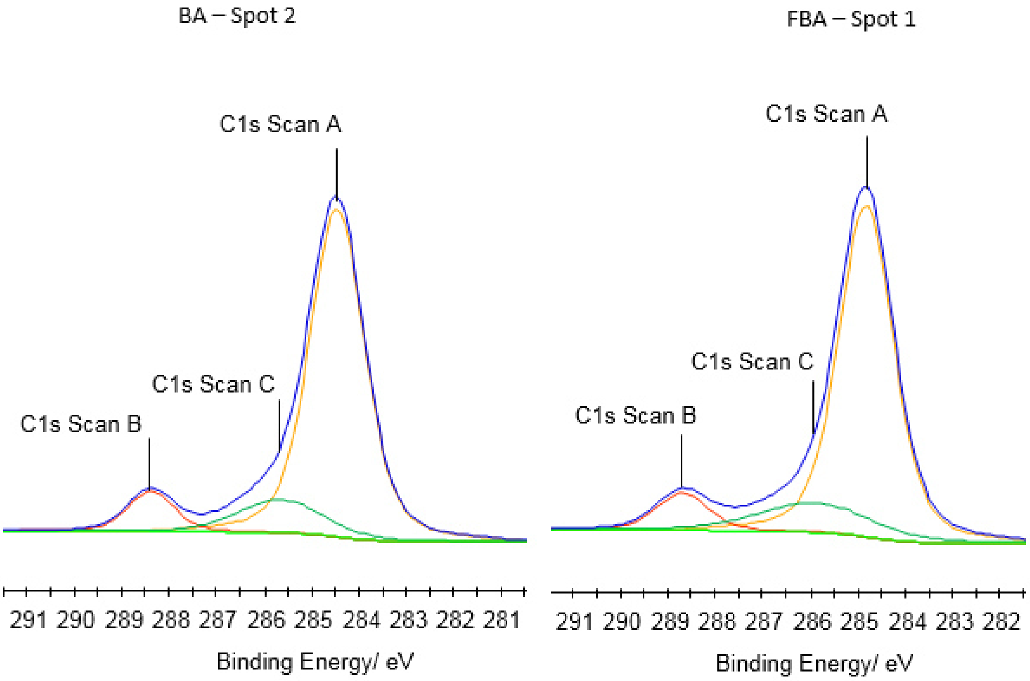

Figure 33: Comparison C1s Scan – BA and FBA coated TiO_X.

- 4-Methoxy benzoic acid

Table 11 shows the XPS data of V_2O_5 coated with MBA. The C1s signal of the methoxy group appears at around 286 eV, depending on the chemical environment.[78] The C1s Scan C signals are considerably larger than the signals obtained from BA. Hence, it can be assumed, that the signal of the methoxy group is overlayed by the C1s Scan C signal.

Table 11: XPS data of V_2O_5 coated with MBA.

	Spot 1		*Spot 2*	
	Atomic %	**Peak Binding Energy/ eV**	**Atomic %**	**Peak Binding Energy/ eV**
C1s Scan A	14.66	284.61	15.70	284.62
C1s Scan B	1.70	288.98	1.91	289.15
C1s Scan C	6.49	285.73	6.39	285.86
O1s Scan A	38.77	530.68	38.13	530.64
O1s Scan B	15.21	531.45	14.80	531.44
N1s Scan A	1.35	400.45	1.04	400.38
N1s Scan B	0.86	402.16	1.25	402.14
V2p3 Scan A	20.94	517.76	20.77	517.76

Figure 34 shows the corrseponding C1s signals of BA and MBA.

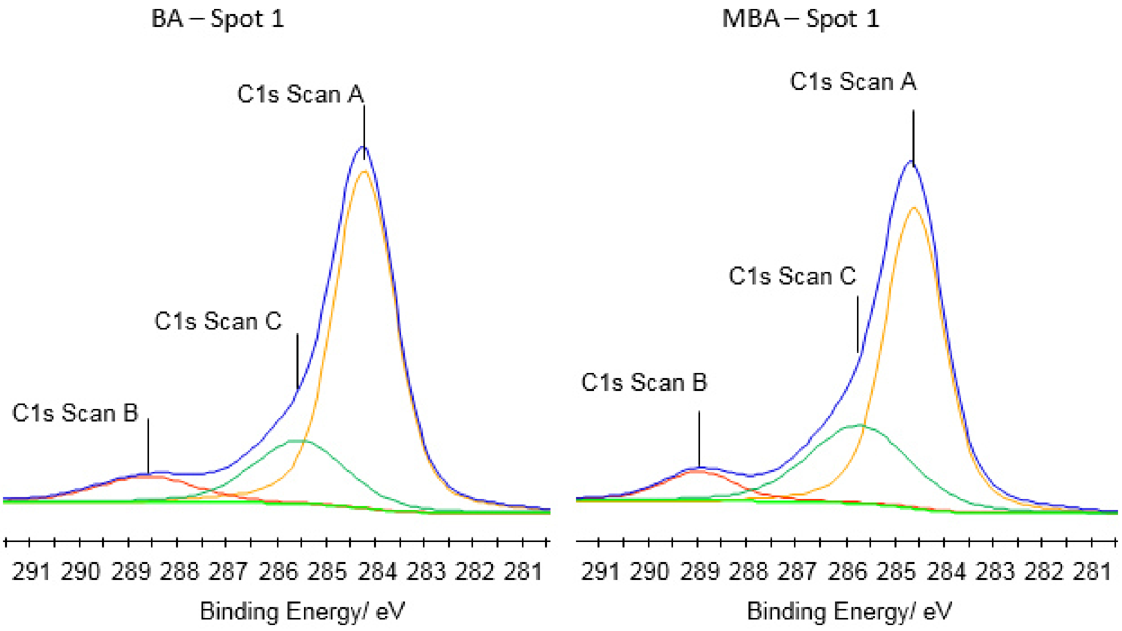

Figure 34: Comparison of the C1s Scans – BA and MBA coated V_2O_5.

The data of the TiO_X coated MBA substrate are shown in Table 12. Here, too the signal of the methoxy group is overlayed by the other signals.

Table 12: XPS data of TiO_X coated with MBA.

	Spot 1		*Spot 2*	
	Atomic %	**Peak Binding Energy/ eV**	**Atomic %**	**Peak Binding Energy/ eV**
C1s Scan A	7.54	284.07	10.03	284.11
C1s Scan B	4.19	287.76	3.5	288.28
C1s Scan C	12.32	284.91	3.93	285.65
O1s Scan A	44.86	529.24	50.11	529.24
O1s Scan B	9.43	530.84	8.22	530.64
N1s Scan A	0.16	399.14	0.14	398.75
N1s Scan B	-	-	0.17	400.49
Ti2p3 Scan A	21.50	458.00	23.89	458.02

Interestingly, here is a shift in the C1s Scan B and Scan C signals (see Figure 35). Possible reason could be a non-uniform coverage with MBA.

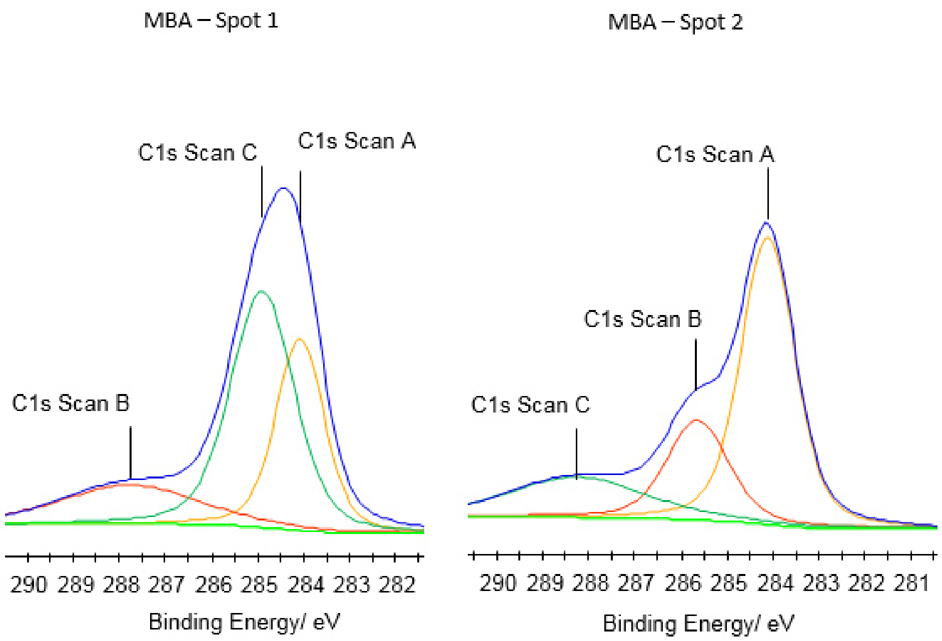

Figure 35: Comparison of the C1s signals (spot 1 and 2) of the MBA coated TiO_X.

- 4-Cyano benzoic acid

According to literature,[78] the N*≡C signal appears at 399.3 eV. Hence, the N1s Scan A signal can be associated with the signal of the nitrogen from the cyano group. Furthermore, here the nitrogen concentration is higher for both signals (on average 30% for N1s Scan A and 36% for N1s Scan B, see Table 13). All C1s and O1s signals can be assigned to the aromatic system or the carboxyl group of the benzoic acid (see Figure 36).

Table 13: XPS data of V_2O_5 coated with CBA.

	Spot 1		*Spot 2*	
	Atomic %	**Peak Binding Energy/ eV**	**Atomic %**	**Peak Binding Energy/ eV**
C1s Scan A	17.64	284.02	16.90	284.04
C1s Scan B	1.89	288.18	1.74	288.32
C1s Scan C	6.99	285.10	6.95	285.16
O1s Scan A	37.74	530.02	35.87	530.01
O1s Scan B	13.29	530.88	15.37	530.85
N1s Scan A	1.44	399.42	1.61	399.26
N1s Scan B	1.04	401.73	1.22	401.56
V2p3 Scan A	19.97	517.10	20.34	517.10

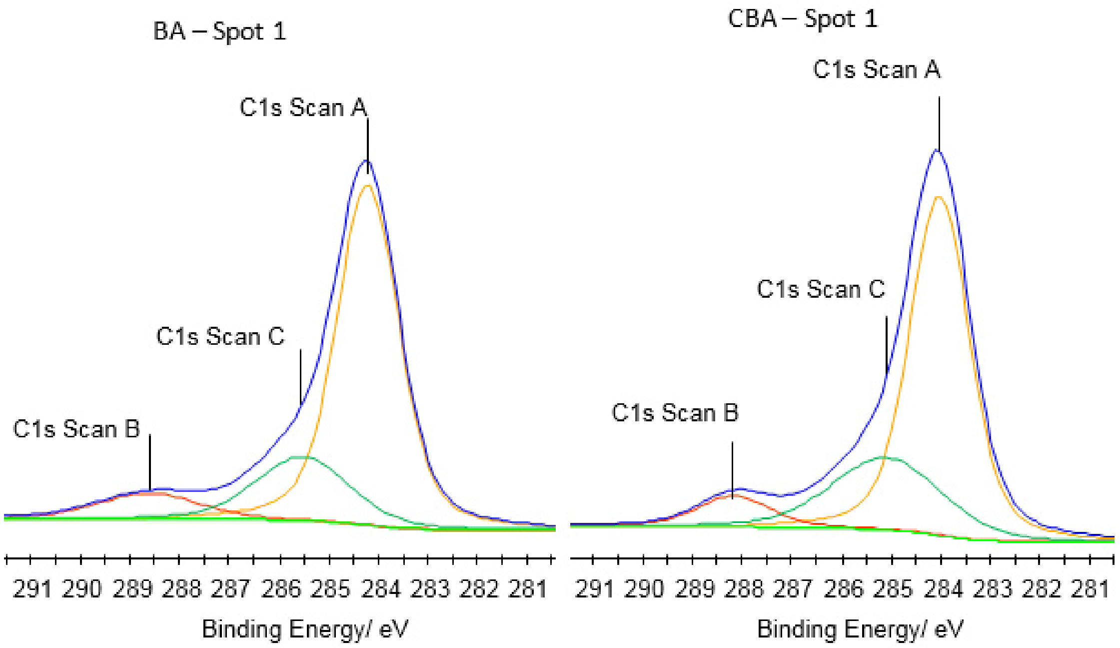

Figure 36: Comparison of the C1s Scans – BA and CBA coated V_2O_5.

The CBA coated TiO_X shows on average a four times higher N1s signal than the other coated TiO_X substrates (see Table 14).

Table 14: XPS data of CBA coated TiO_X.

	Spot 1		*Spot 2*	
	Atomic %	**Peak Binding Energy/ eV**	**Atomic %**	**Peak Binding Energy/ eV**
C1s Scan A	13.91	285.47	7.87	285.44
C1s Scan B	1.86	289.20	1.73	289.56
C1s Scan C	3.18	286.87	7.75	268.36
O1s Scan A	47.92	530.66	49.97	530.67
O1s Scan B	8.91	531.98	7.81	532.05
N1s Scan A	1.26	400.12	1.28	400.13
N1s Scan B	-	-	-	-
Ti2p3 Scan A	22.96	459.28	23.59	459.37

Figure 37 shows the comparison if the BA and CBA coated TiO_X. The different signals are due to an inhomogeneous coating with the SAM. The signal from the carbon of the cyano group may be overlayed by the other carbon signals.

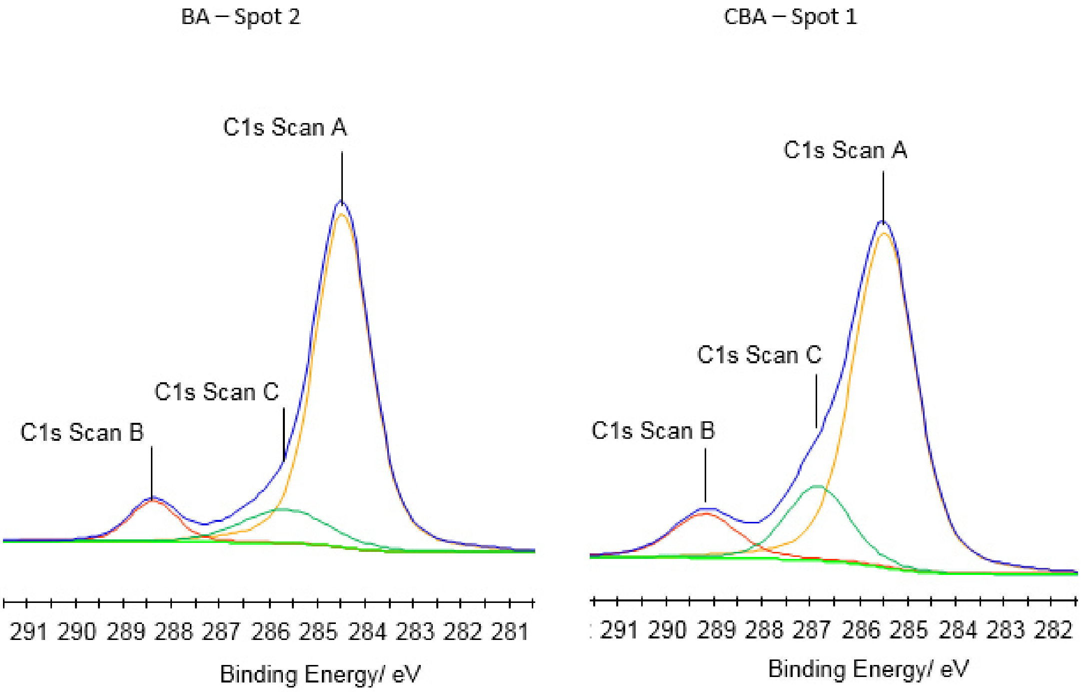

Figure 37: Comparison of the C1s Scans – BA and CBA coated TiO_X.

- 4-*tert*-Butyl benzoic acid

According to literature,[78] there are two signals originating from the *tert*-butyl group ($C^*(CH_3)_3$: ≈287 eV and $C(C^*H_3)_3$): ≈ 285 eV). As can be seen in Table 15, these signals are absent, due to the fact, that they are overlayed by the other C1s signals.

Table 15: XPS data of V_2O_5 coated with tBBA.

	Spot 1		*Spot 2*	
	Atomic %	**Peak Binding Energy/ eV**	**Atomic %**	**Peak Binding Energy/ eV**
C1s Scan A	16.27	284.57	18.19	284.30
C1s Scan B	2.18	289.14	2.27	288.75
C1s Scan C	5.76	285.88	2.97	285.93
O1s Scan A	39.42	530.63	39.24	530.33
O1s Scan B	13.62	531.46	14.23	531.16
N1s Scan A	1.18	400.33	1.03	399.98
N1s Scan B	0.81	402.12	0.69	401.97
V2p3 Scan A	20.76	517.70	21.39	517.41

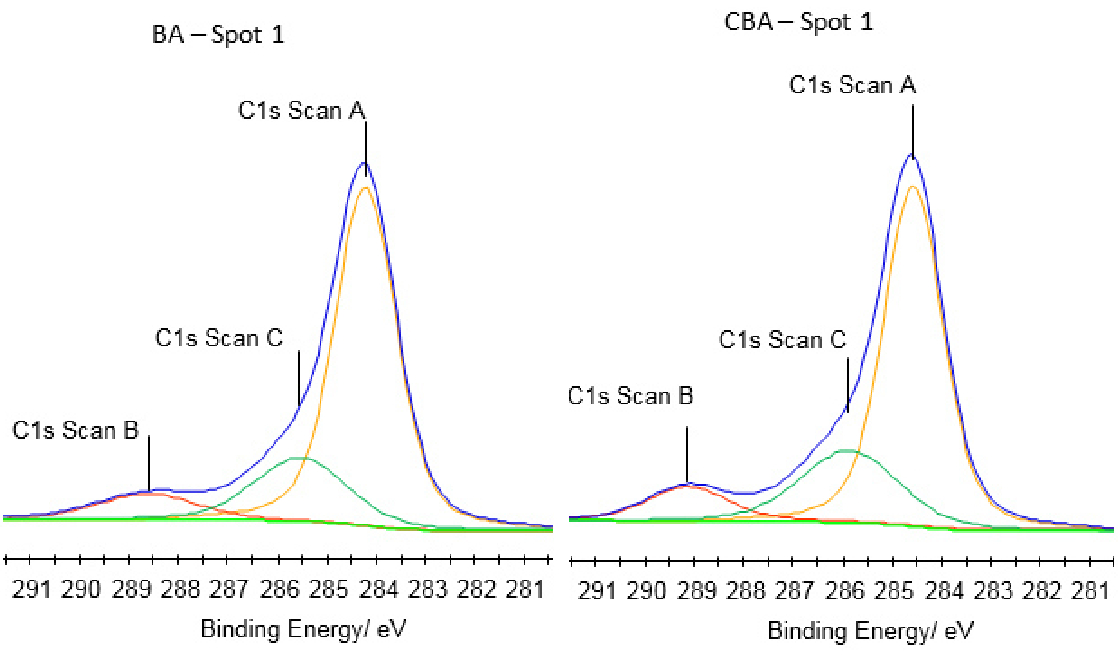

Figure 38: Comparison of the C1s Scans – BA and tBBA coated V_2O_5.

Table 16 shows the XPS data of tBBA coated TiO_X. In addition, here, the peaks of the *tert*-butyl group are overlayed by the other C1s signals.

Table 16: XPS data of tBBA coated TiO_X.

	Spot 1		*Spot 2*	
	Atomic %	**Peak Binding Energy/ eV**	**Atomic %**	**Peak Binding Energy/ eV**
C1s Scan A	15.96	285.21	12.14	285.12
C1s Scan B	3.57	289.30	1.64	288.94
C1s Scan C	1.46	286.43	6.42	285.73
O1s Scan A	48.19	530.32	47.69	530.28
O1s Scan B	7.33	531.60	8.63	531.55
N1s Scan A	0.51	400.76	0.45	400.26
N1s Scan B	-	-	-	-
Ti2p3 Scan A	22.98	459.09	23.04	459.03

In Figure 39, the C1s signal of spot 1 is shown. The change in the peak shapes (Scan B and C) may be due to the *tert*-butyl group.

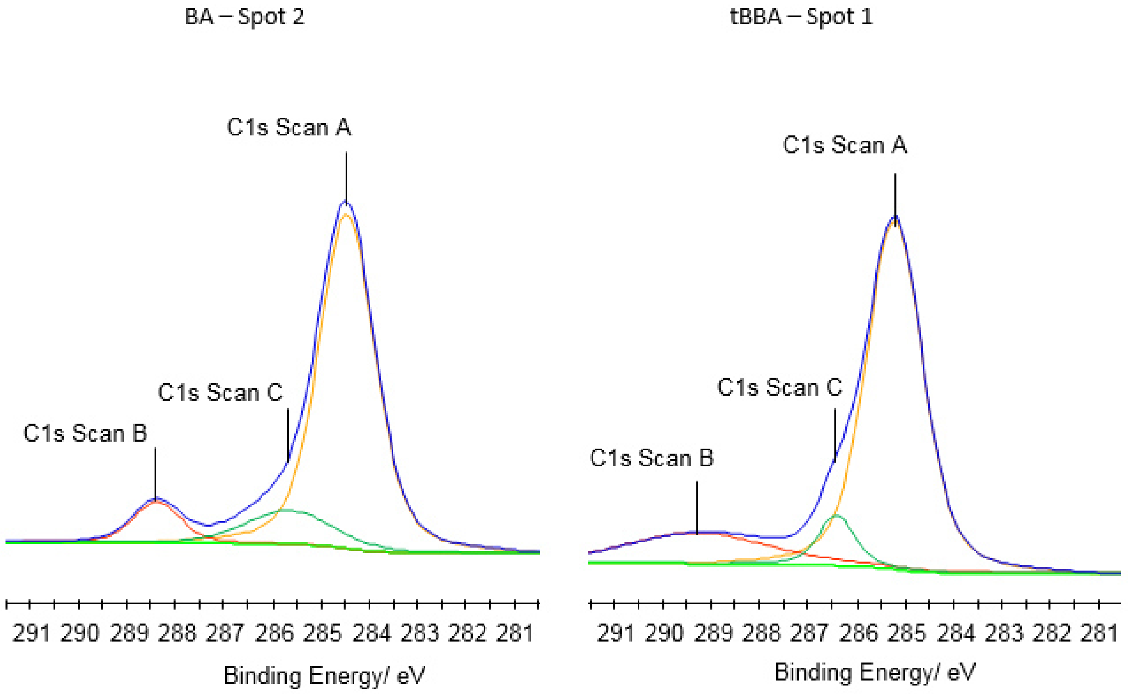

Figure 39: Comparison of the C1s Scans – BA and tBBA coated TiO_X.

- Phosphonic acids

Next to the coating with the molecules mentioned above, TiO_X was coated with two phosphonic acids (detailed information is given in Chapter 4.2.). The results of the XPS measurements are shown in Table 17.

Table 17: XPS data of TiOX coated with 1-Tetradecylphosphonic acid and 4-Phosphonobutyric acid.

TiO_X with 1-Tetradecylphosphonic acid				
	Spot 1		*Spot 2*	
	Atomic %	**Peak Binding Energy/ eV**	**Atomic %**	**Peak Binding Energy/ eV**
C1s Scan A	27.00	284.91	21.31	284.84
O1s Scan A	50.23	530.03	54.86	529.92
Ti2p3 Scan A	20.82	458.80	22.28	458.31
P2p Scan A	1.94	133.18	1.55	133.11
TiO_X with 4-Phosphonobutyric acid				
	Spot 1		*Spot 2*	
	Atomic %	**Peak Binding Energy/ eV**	**Atomic %**	**Peak Binding Energy/ eV**
C1s Scan A	10.98	285.23	10.80	285.20
O1s Scan A	62.76	530.14	62.90	530.14
Ti2p3 Scan A	24.66	458.92	24.89	458.92
P2p Scan A	1.60	133.47	1.41	133.30

On both substrates, the coating with the phosphonic acids was successful. The ratio of C/P in 1-tetradecylphosphonic acid is 14:1; in fact, it is a little lower (13.5:1). In contrast, the ration of C/P in 4-phosphonobutyric acid is 4:1; based on the measured data, the ratio is 7:1. Reason for this may be carbon impurities.

3.3. SAMs in Solar Cells

This chapter deals with the influence of the SAMs on the characteristic parameters of a solar cell. Various effects regarding to the voltage and the current density occur, due to the changes in the wettability and the different dipole moments of the SAMs used.

3.3.1. SAMs on V_2O_5 in a Normal Device Architecture

Self-assembling monolayers consisting of BA and its derivates, are applied on V_2O_5 as a hole transport layer. Therefore, the V_2O_5 layer is prepared as described before (see Chapter 3.) For a complete analysis, devices also with PEDOT:PSS as HTL are fabricated. Due to the fact, that the V_2O_5 layer is very prone to detach from ITO, no alcohol as solvent could be used. A suitable solvent is acetone. The active film consists of a blend of P3HT:PCBM followed by an aluminum layer as metal contact. Detailed information about the device fabrication are given in Chapter 4.

Figure 40 shows the arrangement of the various layers in a normal solar cell device.

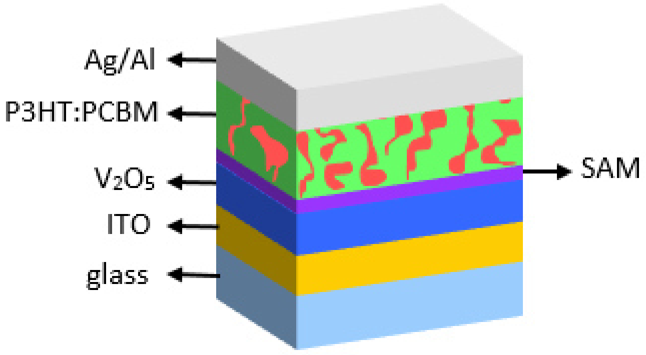

Figure 40: Normal device architecture with V_2O_5 and SAMs.

Hydroxyl groups located on the surface of vanadium pentoxide cause a very hydrophilic atmosphere. These OH- groups originate on the one hand from a possible incomplete conversion of the precursor solution and on the other hand by the atmospheric humidity. To keep the problem of impurity atoms and molecules as low as possible, the V_2O_5 coated substrates are treated by oxygen plasma.

In addition to the changes of the wettability, another influencing factor of a self-assembling monolayer on the V_2O_5 layer is the change of the work function. According to literature, the WF increases by the use of self-assembling molecules with electron-withdrawing groups and decreases by molecules with electron-donating groups. To investigate this effect, SAMs with both groups are used. The dipole moments of the molecules used are summarized in Table 18.

Table 18: Dipole moments of the SAMs used.

	Dipole Moment/ D					
	Ref. 79	*Ref. 57*	*Ref.59*	*Ref.60*	*Ref.53*	*Ref.54*
MBA	-3.9*	-3.7	-1.2	-1.45	-3.9	-3.9
BA	-2*	-2.0	0.0		-2.1	-2.0
CBA	+3.7*	+3.7	+4.1		+3.4	+3.7
FBA				+1.55		
tBBA				-0.55		

* gas-phase

The mismatch in the dipole moments results from the fact, that they are measured in different media. Even if the strength of the dipole moments vary, it is clear to see, that MBA and tBBA as well as BA have a negative and FBA and CBA a positive one.

Figure 41 shows the energy levels of the materials used in the normal device architecture with V_2O_5 (WF = 4.7 eV),[29] as well as with PEDOT:PSS (WF = 5.0-5.2 eV)[12,13,15,27-29,35,40,43] as a HTL.

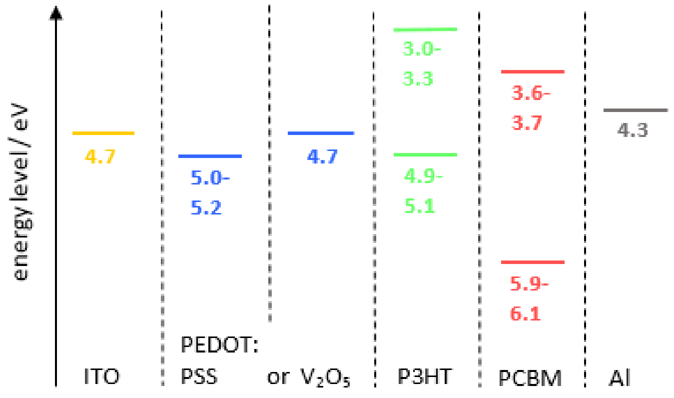

Figure 41: Energy levels of materials used.

First, devices with SAMs are prepared via approach #1. As an illustration, the IV-curves in the dark of the cells with the best PCE values are shown in Figure 42. Figure 43 shows the corresponding curves measured under illumination.

According to the data of McGehee,[53] the charge carrier concentration increases due to the better adjustment of the energy levels of the polymer and the buffer layer with respect to the dipole moment. As a result, the electrons and holes recombine faster leading to a sooner turn-on of the dark current.

For a better comparison, the curves of the devices with PEDOT:PSS and pure V_2O_5 as a hole transport layer as well as pure V_2O_5 rinsed with acetone are displayed.

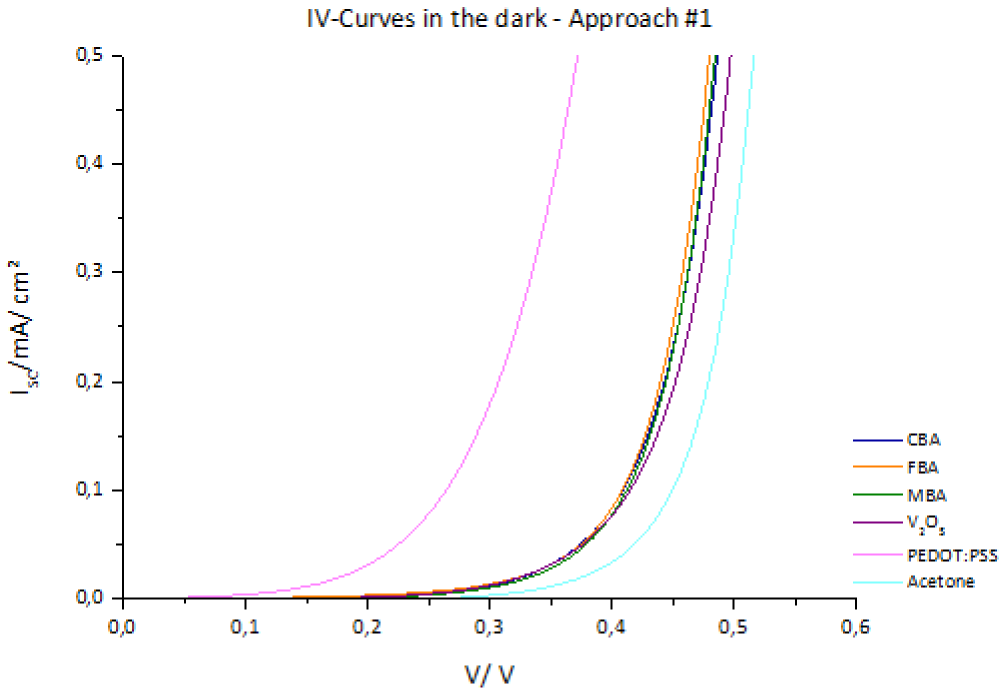

Figure 42: IV-Curves in the dark – approach #1.

All SAMs used as well as the V_2O_5 layer treated with acetone show higher values of the turn-on of the dark current. The solar cells with PEDOT:PSS as HTL have the earliest turn-on, which indicates, that the charge carrier concentration is the highest in these devices. Noticeable is the voltage observed in devices with a pure V_2O_5 layer treated with acetone. It is slightly higher than that of the SAMs. All the curves of the devices with SAMs are all located in the same area. According to these data, the devices with PEDOT:PSS as HTL have the highest concentration of free charge carriers, followed by

V_2O_5 and SAM coated V_2O_5. The enhanced value of acetone suggests that the solvent has an influence on the characteristics of the solar cells. The latter turn-on of the dark current in these devices leads to a decreased I_{SC} in IV-curves measured under illumination (see Figure 43). Solar cells with V_2O_5 rinsed with acetone have the lowest amount of charge carriers, which is seen in the decreased value of the I_{SC}.

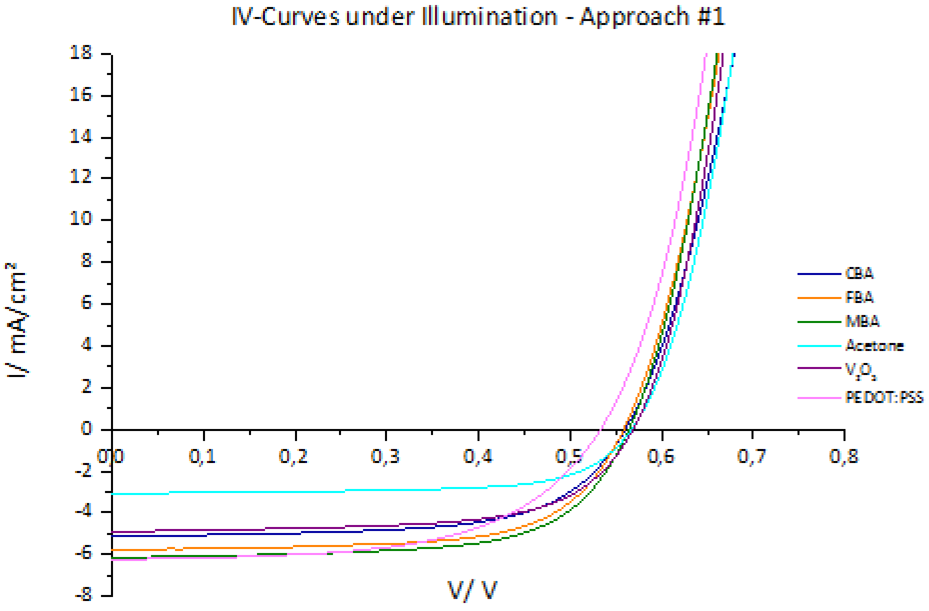

Figure 43: IV-Curves under illumination – approach #1.

The former turn-on of the dark current leads to a lower V_{OC}. Table 19 shows the average cell parameters. It can be seen, that the average V_{OC} values do correspond with the selected data above. The device with PEDOT:PSS as a HTL shows the lowest value of V_{OC} and the one with the V_2O_5 layers treated with acetone the highest value.

Table 19: Characteristic parameters of solar cells using approach #1 (average of 10 devices).

	V_{OC}/ V	±	**I_{SC}/ mA/cm²**	±	**FF/ %**	±	**η/ %**	±
PEDOT:PSS	0.500	0.062	5.81	0.47	59.0	1.2	1.69	0.14
V_2O_5	0.561	0.004	3.18	0.82	65.0	1.0	1.15	0.29
acetone	0.571	0.006	3.19	0.31	66.5	1.8	1.20	0.13
CBA	0.559	0.006	5.01	0.21	62.6	1.4	1.74	0.05
FBA	0.557	0.009	4.24	0.98	66.3	1.4	1.55	0.34
MBA	0.560	0.004	5.31	1.12	66.4	4.7	1.95	0.29

The FBA treated solar cells also show a slightly lower current density, which in turn is due to the poor adhesion properties of FBA on V_2O_5. In the case of CBA and MBA, no significant difference of the I_{SC} is apparent. However, all devices with the self-assembling monolayers show higher values of the current density, which leads to enhanced PCE values. For a better visualization, the average values of V_{OC} and I_{SC} are summarized in Figure 44.

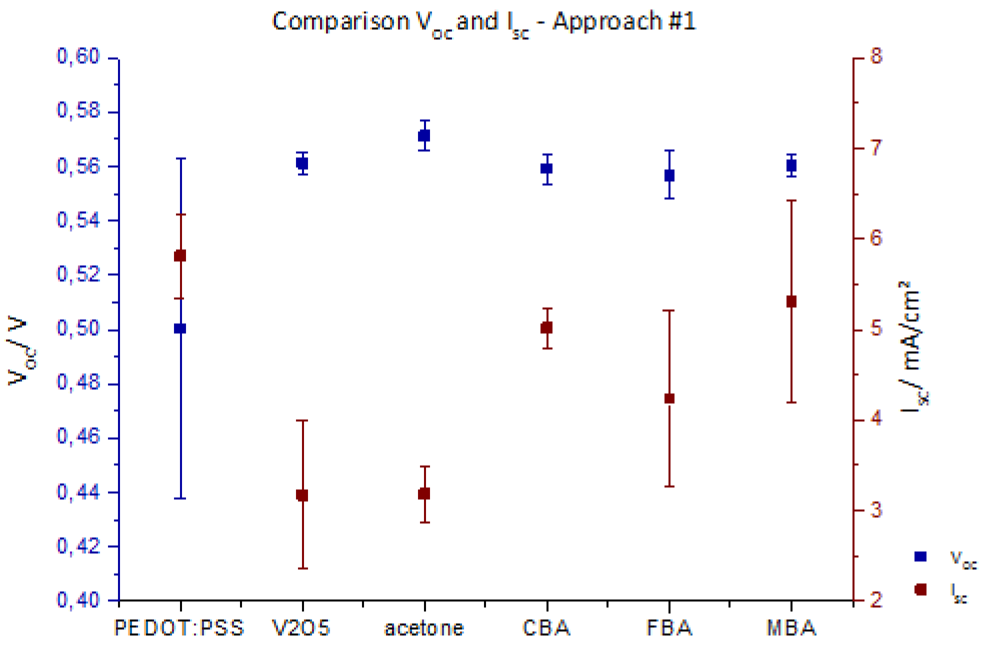

Figure 44: Comparison V_{OC} and I_{SC} – approach #1

According to Bedis,[46] CBA with a positive dipole moment should have a higher I_{SC} and a slightly enhanced V_{OC} and MBA should have a decreased V_{OC}. The work of Jones et al.[61] shows, that the V_{OC} is increased using SAMs with both, negative and positive, dipole moments.

Based on the data above, there is no influence of the SAMs` dipole moment on the V_{OC} and I_{SC}. The increased values of the current density are probably caused by the better wettability of the photoactive layer resulting in a higher charge transfer rate.[52,61]

In the following, devices using approach #2 and additionally to the SAMs used before, here the influence of tBBA and BA are investigated.

The IV-curves of the best devices are shown in Figure 45 (in the dark) and in Figure 46 (under illumination).

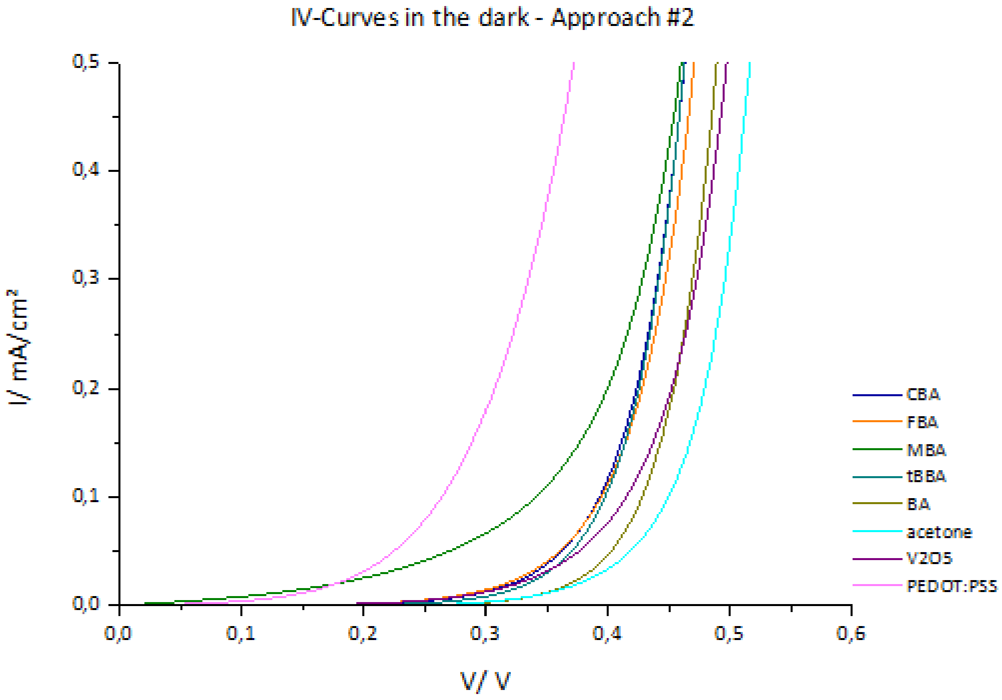

Figure 45: IV-Curves in the dark – approach #2.

As a reference, the devices with PEDOT:PSS, pure V_2O_5 and pure V_2O_5 treated with acetone are used.

However, in contrast to approach #1, the MBA treated device has, an earlier turn-on, followed by CBA and FBA. As seen in Figure 46, CBA and FBA coated V_2O_5 solar cells have a higher current density than the other devices.

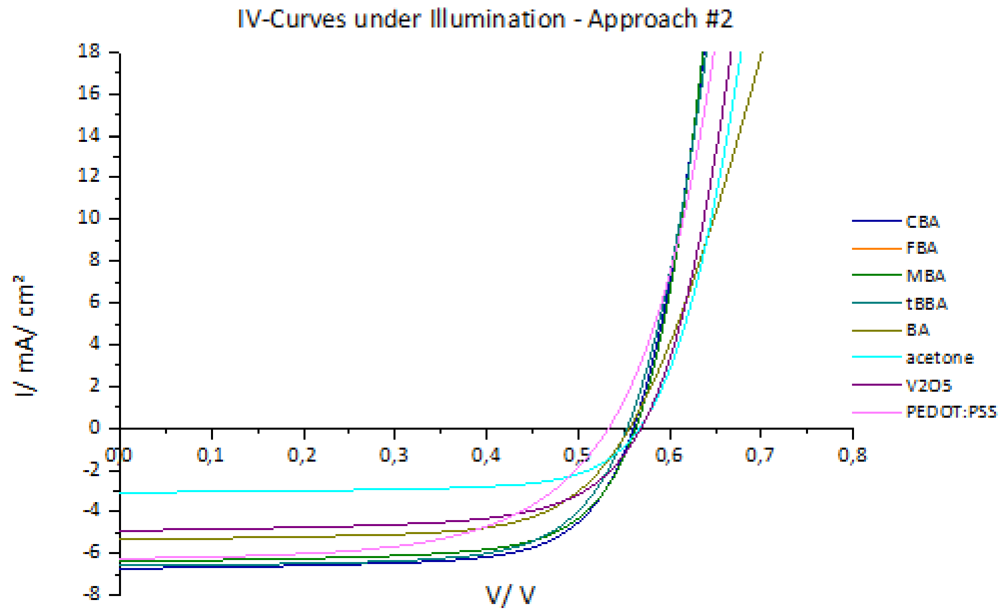

Figure 46: IV-Curves under illumination – approach #2.

Since here only the washing process is different, the results (see Table 20) should be comparable with the data from approach #1. As before, the V_{OC} values are all in the same range. In addition, the I_{SC} values are higher compared to the pure V_2O_5.However, the MBA treated devices of the first approach supply the highest I_{SC}, here it is the lowest. Solar cells with CBA as a self-assembling monolayer deliver the highest I_{SC} values, those with FBA average values (FBA treated devices show the lowest values in case of approach #1).

Table 20: Characteristic parameters – approach #2 (average of 10 devices).

	V_{OC}/ V	±	**I_{SC}/ mA/cm^2**	±	**FF/ %**	±	**η/ %**	±
PEDOT:PSS	0.500	0.062	5.81	0.49	59.0	1.2	1.69	0.14
V_2O_5	0.561	0.004	3.18	0.82	65.0	1.0	1.15	0.29
acetone	0.571	0.006	3.19	0.31	66.5	1.8	1.20	0.13
CBA	0.553	0.008	6.74	0.09	66.6	1.5	2.47	0.08
FBA	0.557	0.005	6.01	0.29	65.8	1.0	2.25	0.14
MBA	0.557	0.005	4.62	0.27	67.1	1.3	1.72	0.09
tBBA	0.551	0.006	6.31	0.20	67.9	0.7	2.35	0.07
BA	0.555	0.000	5.15	0.46	63.8	2.8	1.81	0.13

The standard variance is much lower here, which indicates that the monolayer is more homogenous. This is also seen in the values of the water contact angle.

The different I_{SC} values of the devices with the individual SAMs are also reflected in the values of the series resistance (see Table 21).

Table 21: Average series resistance – approach #1 and #2

Approach #1			Approach #2		
	R_S/ Ω cm²	±		**R_S/ Ω cm²**	±
PEDOT:PSS	12.96	0.41	*PEDOT:PSS*	12.96	0.41
V_2O_5	14.50	1.73	*V_2O_5*	14.50	1.73
Acetone	17.79	3.22	*Acetone*	17.79	3.22
CBA	12.78	0.50	*CBA*	7.74	0.69
FBA	14.21	2.45	*FBA*	8.43	0.89
MBA	10.55	0.85	*MBA*	11.62	2.05
			tBBA	8.46	0.72
			BA	14.23	1.63

In approach #1, devices with FBA have the same series resistance than pure V_2O_5. Solar cells with CBA and MBA show only a slightly decrease in R_S. In approach #2, FBA treated solar cells have besides tBBA and CBA the lowest series resistance. Here, devices with BA show no change in R_S.

According to Kim et al.[60] the resistance of solar cells with FBA should have a higher resistance because of the bigger P3HT and PCBM domains and those of tBBA and MBA treated ones should have lower values.

For a better comparison of the influence of acetone on the performance of solar cells, another experimental series with THF as solvent was performed. The obtained data are summarized in Table 22.

Table 22: Solar cell parameters of devices with acetone and THF (average of 5 devices).

	VOC/ V	ISC/ mA/cm²	FF/ %	η/ %
CBA in acetone	0.553	6.74	66.6	2.47
CBA in THF	0.541	5.40	67.1	1.94
FBA in acetone	0.557	6.00	65.8	2.25
FBA in THF	0.553	4.84	68.8	1.84
MBA in acetone	0.557	4.62	67.1	1.72
MBA in THF	0.553	5.02	69.2	1.91
tBBA in acetone	0.551	6.31	67.9	2.35
tBBA in THF	0.561	5.11	69.6	1.98
BA in acetone	0.555	5.15	63.8	1.81
BA in THF	0.537	4.22	65.2	1.47

Due to these data, there is an effect of the solvent on the performance of solar cells. The solvent can influence the order of the self-assembling molecules and there is the possibility that it changes the V_2O_5 surface itself.

The received data suggest that the different dipole moments of the SAMs used do not influence the voltage and the current density. Reason for this could be the above-mentioned partial coating of the V_2O_5 surface. The enhanced current could be attributed to the better structuring of the active layer with respect to the size of the donor and acceptor domains (according to Kim et al.[60]).

Another explanation for the better performance of the solar cells could be the modification of the V_2O_5 surface. The SAMs used increase the contact angles values and so the surface exhibit a more hydrophobic character. This leads to a better coating of the photoactive film resulting in an improved charge transport and a better charge separation. Although the contact angles are higher with THF as a solvent, the obtained values of V_{OC}, I_{SC} as well as the fill factor are decreased.

3.3.1. SAMs on TiO_X in an Inverted Architecture

This chapter deals with the effects of SAMs on two differently prepared TiO_X layers. In addition to the benzoic acid and its derivates, two phosphonic acids, 1-tetradecylphosphonic acid (tDPA) and 4-phosphonobutyric acid (PBA) (see Figure 47) are used.

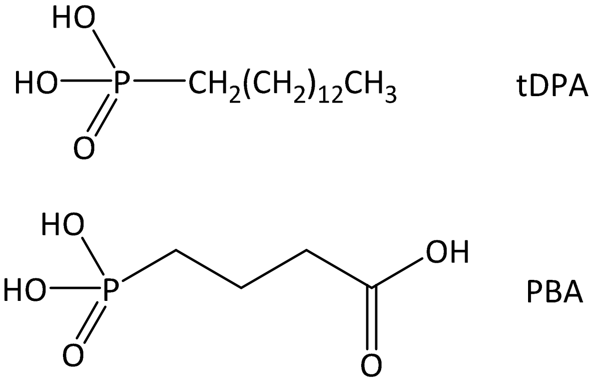

Figure 47: Structure of the phosphonic acids used in the inverted architecture.

Just as in the normal architecture, an oxygen plasma activates the buffer layer. After that, the preparation with the SAMs occurs via two different routes using methanol as a solvent. P3HT:PCBM forms the active layer. As hole transport layer two different PEDOT:PSS solutions as well as molybdenum oxide (MoO_3)[80] are used. Reason for the different HTL layers is the poor coating of PEDOT:PSS – especially if it is applied via doctor blading.

For the metal contact, only silver is applied. Detailed information about the device production is given in chapter 4.

Figure 48 shows the architecture for an inverted device.

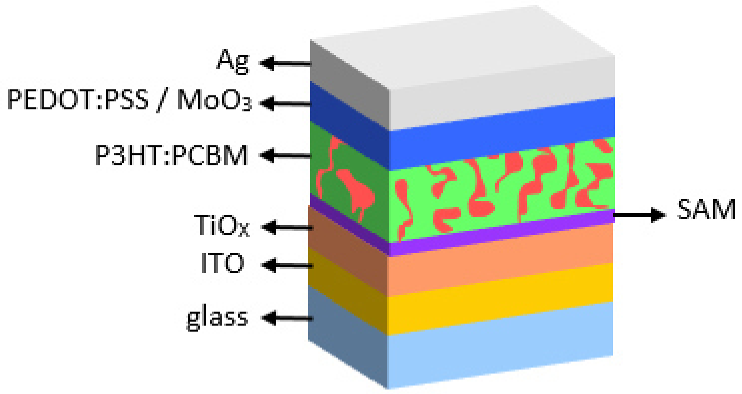

Figure 48: Architecture for inverted devices.

The influencing factors of SAMs on the TiO_X layer are the same as on V_2O_5: changing of the wetting properties by increase of the contact angle and modification of the work function. The WF of the materials used are shown in Figure 49.

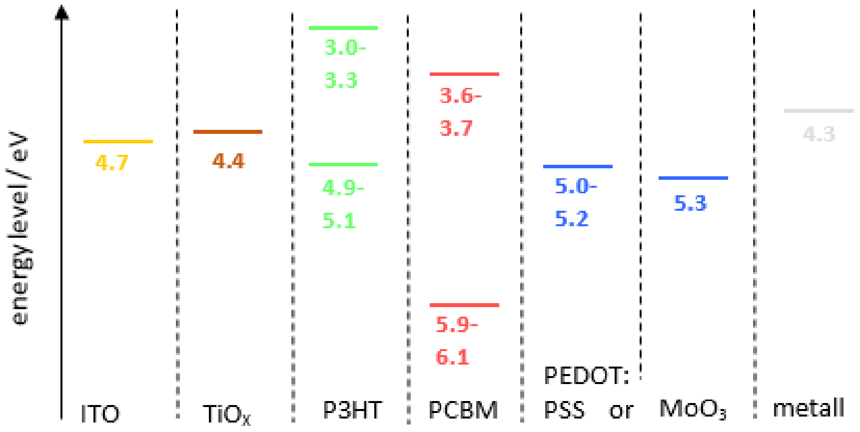

Figure 49: WF of materials used in the inverted architecture.

In the first approach, the TiO_X layer is formed from the precursor solution. As HTL, a PEDOT:PSS solution in isopropanol with Dynol as adhesion medium, is used. The SAM coating is carried out via spin coater to remove the non-chemisorbed molecules, the substrates are rinsed with 10 ml pure MeOH (detailed information are given in Chapter 4.1.). Only data from three SAMs are obtained, since the adhesion of the PEDOT:PSS on the active layer is not homogenous. The average characteristic parameters of the fabricated devices are shown in Table 23.

Table 23: Solar cell parameters using approach #1 (average of 5devices).

	V_{OC}/ V	±	I_{SC}/ mA/cm²	±	FF/ %	±	η/ %	±
TiO_X	0.587	0.008	6.97	0.47	57.3	1.3	2.32	0.17
CBA	0.593	0.018	7.09	0.95	53.1	7.2	2.18	0.17
FBA	0.567	0.015	7.28	0.23	53.3	1.1	2.19	0.09
MBA	0.579	0.031	7.71	0.43	58.6	4.7	2.62	0.47

According to literature,[53] MBA with a negative dipole moment should have a lower current density and an increased voltage. As seen in the table above, it is just the opposite here. MBA has the highest I_{SC} values and CBA, with the largest positive dipole moment, the highest voltage. However, these data agree with the values of Kim et al.[60], there, MBA has also the highest I_{SC}, which is due to the smaller P3HT and PCBM domains.

In the next approach, a PEDOT:PSS solution, which has been developed specifically for the inverse architecture, is used. It is applied via spin coater. The remaining layers are the same as above. Table 24 shows the average values of V_{OC}, I_{SC}, FF and PCE.

Table 24: Average solar cell parameters – approach #2 (average of 10 devices).

	V_{OC}/ V	±	I_{SC}/ mA/cm²	±	FF/ %	±	η/ %	±
MeOH	0.557	0.008	7.71	0.42	55.4	1.9	2.37	0.05
CBA	0.561	0.011	8.37	0.20	53.1	1.7	2.47	0.13
FBA	0.581	0.027	7.38	0.35	31.8	2.3	1.36	0.07
MBA	0.569	0.006	7.62	0.29	53.3	1.2	2.31	0.08
tBBA	0.555	0.012	8.18	0.33	53.9	4.0	2.43	0.17
BA	0.549	0.006	7.90	0.44	57.7	3.2	2.47	0.11

CBA with a strong positive dipolar moment and tBBA with a weak negative one, have the highest current density. FBA shows the highest voltage, CBA, however, the lowest voltage. Although, the values of voltage and current density coming from the FBA treated devices are comparable to the other SAMs, the fill factor is very low. Here, MeOH, in contrast to acetone in the normal device architecture, has no negative effect on the current density.

In the IV-curves under illumination (see Figure 50), one can see why the FF has such a low value. Based on this curve, there must be defects in the structuring of this device, resulting in a low photovoltaic activity. Reason for this may be a low charge carrier transport in combination with a high charge recombination rate.

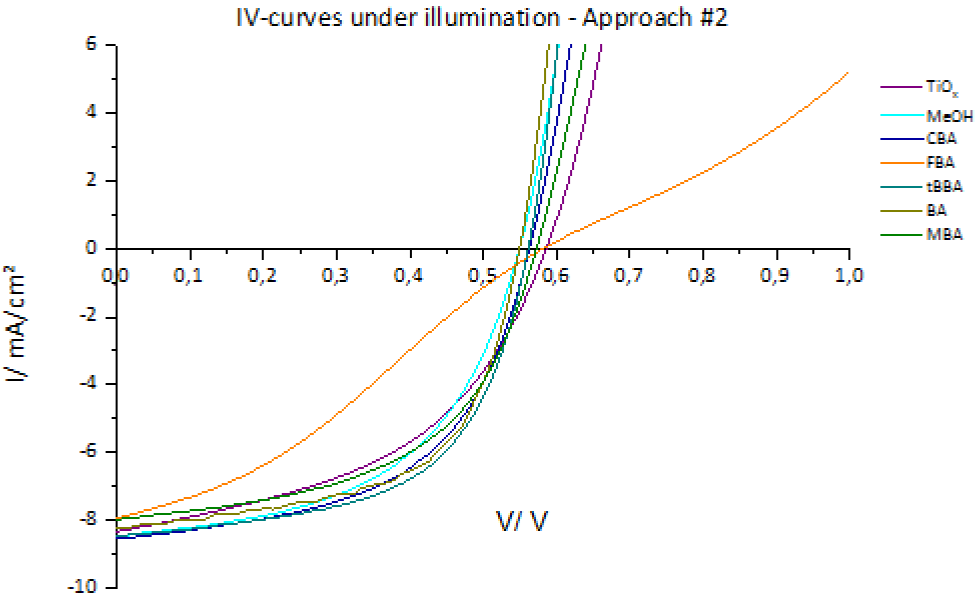

Figure 50: IV-Curves under illumination – approach #2.

It cannot be assumed, that an increased charge carrier density due to a better alignment of the energy levels is given.

Next, PEDOT:PSS as electron transport layer is replaced by MoO_3. A 5 nm thin layer thereof is vapor deposited on the photoactive film. The measured solar cell characteristics are summarized in Table 25. Only one device with FBA coated TiO_X shows photovoltaic activity.

Table 25: Characteristic parameters of solar cells using approach #3 (average of 5 devices).

	V_{OC}/ V	±	**I_{SC}/ mA/cm²**	±	**FF/ %**	±	**η/ %**	±
TiO_X	0.515	0.027	7.60	0.18	48.7	1.8	1.89	0.12
MeOH	0.545	0.019	7.83	0.39	51.5	2.4	2.18	0.13
CBA	0.449	0.025	7.77	0.74	45.0	1.7	1.54	0.10
FBA	0.445		8.40		43.6		1.61	
tBBA	0.525	0.044	7.93	0.30	52.5	4.6	2.20	0.42
BA	0.561	0.006	7.73	0.41	53.4	2.1	2.31	0.22
MBA	0.565	0.000	8.14	0.48	59.2	0.5	2.70	0.14

Figure 51 shows the IV-curves under illumination of the best solar cell of approach #3.

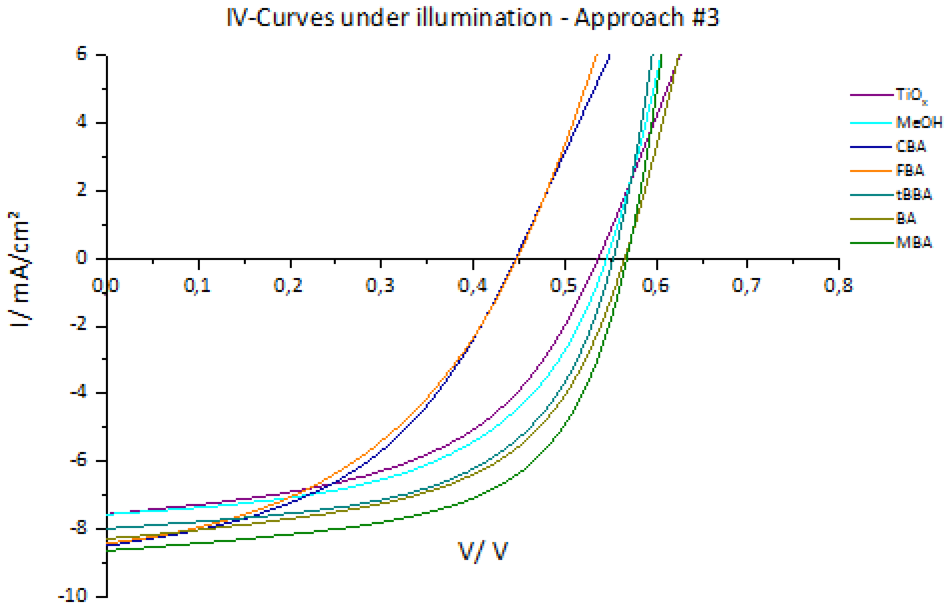

Figure 51: IV-Curves under illumination – approach #3.

Here, the influence of the dipole moment is apparent. According to literature,[53-55] CBA with a positive dipole moment shows a lower voltage. tBBA, BA and MBA with a negative dipole moment have a higher voltage. Here too, MeOH has no negative effect on the I_{SC}. Table 26 shows the comparison of the R_S values of approach #2 and #3. Clearly seen is the correlation between the low FF and the very high value of the series resistance of FBA coated TiO_X in approach #2. All other SAM coated substrates, as well as the MeOH treated show a decreased value.

Table 26: Comparison of R_S – approach #2 and #3.

Approach #2			Approach #3		
	R_S/ Ω cm²	±		**R_S/ Ω cm²**	±
TiO_X	25.74	4.93	*TiO_X*	21.16	5.11
MeOH	10.67	1.16	*MeOH*	15.51	3.01
CBA	11.91	1.13	*CBA*	18.82	1.27
FBA	77.56	11.31	*FBA*	17.70	
tBBA	13.87	5.87	*tBBA*	14.54	8.75
BA	9.86	1.48	*BA*	13.69	2.85
MBA	12.29	1.30	*MBA*	8.18	0.28

Finally, Table 27 shows the characteristic parameters of the solar cells with phosphonobutyric acid. The preparation of devices with tDPA did not work because P3HT:PCBM did not adhere on this layer.

Table 27: Characteristic parameters of PBA treated devices.

	V_{OC}/ V	±	***I_{SC}/ mA/cm²***	±	***FF/ %***	±	***η/ %***	±
TiO_X	0.515	0.027	7.60	0.18	48.7	1.8	1.89	0.12
MeOH	0.545	0.019	7.83	0.39	51.5	2.4	2.18	0.13
PBA	0.563	0.008	7.96	0.39	46.4	1.0	2.06	0.15

The voltage as well as the current density are slightly increased. The FF is lower, which can be seen in Figure 52.

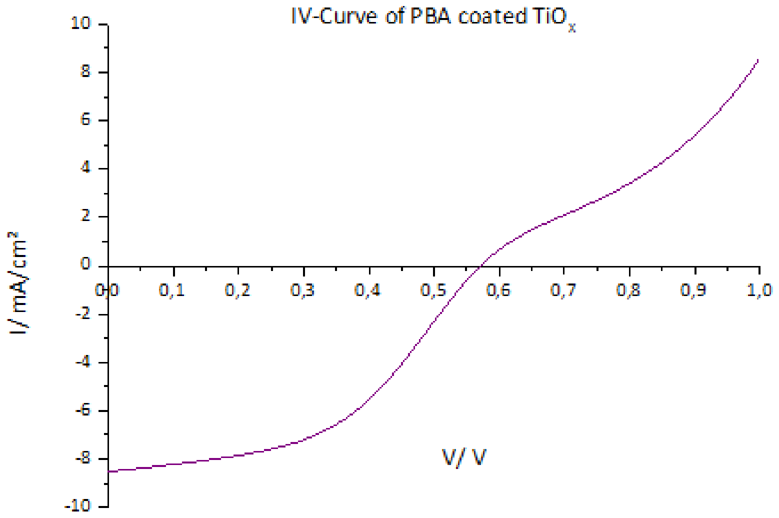

Figure 52: IV-Curve under illumination of PBA coated TiO_X.

4. EXPERIMENTAL PART

All chemicals and solvents (see Table 28) are used without any further purification.

Table 28: Chemicals and solvents used.

Chemicals	**Purity grade**	**Supplier**
Acetone	≥99%	Sigma Aldrich
BA	99%	Fluka
CBA	99%	Sigma Aldrich
Chlorbenzene	≥ 99%	Sigma Aldrich
Dynol	604 Surfactant	AIR Products
FBA	98%	Sigma Aldrich
Isopropanol	99%	Sigma Aldrich
MBA	99%	Sigma Aldrich
Methanol	≥ 99%	Roth
P3HT	RR	Rieke
PBA	techn.	ABCR
PC61BM	99.50%	Solenne
PEDOT:PSS	P VP Al 4083	Heraeus
PEDOT:PSS	HTL Solar	Heraeus
tBBA	99%	Sigma Aldrich
tDPA	98%	Alfa Aesar
THF	99.5%/ H2O ≤ 0.005%	Sigma Aldrich

4.1. Solar Cell Production

4.1.1. Normal Device Architecture

After peel of the protective foil from the ITO, the substrates are rinsed with pure acetone to remove any contaminations. Then ultrasonic treatment (VWR ultrasonic cleaner) cleans them in an isopropanol bath for at least twenty minutes. To ensure a better adhesion of the subsequent layer, the ITO film is activated via oxygen (O_2) plasma etching (Diener Electronics) for three minutes with an O_2 flow of 10 sccm.

- PEDOT:PSS

The aqueous PEDOT:PSS solution is spin coated on the cleaned and activated ITO substrate (30 s, 300 rpm/s, 2500 rpm). Afterwards, this layer is dried at 150 °C in a glove box under inert conditions for 10 minutes.

- Preparation of the V_2O_5 layer:

A 1.25 vol% solution of vanadium(V)oxytriisopropoxid in isopropanol is prepared. This solution is applied on the ITO substrates by spin coating (CT 62 spin coater from Karl Suss Technique S.A.) with the following parameters: 30 s, 300 rpm/s, 2500 rpm. Afterwards the substrates are stored for at least one hour at air until the V_2O_5 network is completely formed (according to literature[41]). Prior to the application of the SAMs the V_2O_5 layer is treated in the plasma etch chamber (parameters are the same as for the ITO activation).

- Preparation of the SAM layer:

The preparation is based on the method of Kim et al.[60] A 1.0 mg/ml solution of the benzoic acid or of the para-substituted derivates in acetone (for V_2O_5) and in MeOH (for TiO_X) is prepared and 0.5 ml thereof are deposited via spin coating (60 s, 300 rpm/s, 4000 rpm) on the respective oxide surface.

To remove the non-chemisorbed molecules the coated substrates are rinsed with 10 ml of the respective solvent. Afterwards, the substrates are dried with a stream of N_2 (approach #1). For approach #2, the coated substrates are covered with 0.5 ml pure acetone and the non-chemisorbed molecules are removed via spin coating (30s, 300 rpm/s, 2500 rpm). Followed by drying with a nitrogen stream.

- Preparation of the photoactive film

P3HT is dissolved in chlorobenzene (10 mg/ml). The solution is stirred for at least one hour to receive a homogeneous system. To obtain an optimal ratio of acceptor and donor (1.0 to 0.8 w% according to literature 45), a pre-calculated amount of the P3HT solution is added to the fullerene acceptor PCBM. This solution is stirred for thirty minutes to obtain a homogenous solution. This precursor is applied to the respective buffer layer via doctor blading (doctor blade 509 MC I by the Erichson Company) with a speed of either 15 mm/s or 20 mm/s at 40°C in the glove box. In order to remove the residual solvent the substrates are dried for several seconds at 60 °C.

- Metal Electrode

The metal contact consisting of a two hundred nm aluminum (Al) layer is applied by deposition at around 1 * 10^{-5} mbar in a thermal evaporation chamber (deposition chamber in glove box system MBraun LABmaster). To get a defined electrode area the substrates are covered with a shadow mask (2 X 2 mm).

- Annealing step

The completed solar cell devices are annealed at 140°C (CAT M. Zippere GmbH) for thirty minutes to obtain a good interpenetrating network.

4.1.2. Inverted Device Architecture

The treatment of the ITO substrates, the preparation if the SAM layer as well as the photoactive film, the vapor deposition of the metal contact and the annealing step are the same as described above.

- Preparation of the TiO_X layer:

First, according to the method used by Ch. Fradler,[81] a 1.0 M solution of titanium propoxide bis (acetylacetonate) is used as a precursor solution. Thereof 30 ml are applied via doctor blading (25 mm/s at 40°C) at air. To convert the precursor into the TiO_X film, the substrates are annealed at 400°C for fifteen minutes under ambient conditions. The second layer preparation occurs via vacuum deposition. For this, metallic Ti is used. The vapor deposition (MED 020) is carried out under ambient conditions to obtain titanium oxide.

The treatment in the plasma etch chamber occurs prior to the coating with the SAMs.

- Preparation of the PEDOT:PSS layer:

The first PEDOT:PSS solution consists of 1 Vol% PEDOT:PSS (Clevios VPAl4083) and 5 Vol% isopropanol and 0.008 Vol% Dynol. It is stirred for at least 15 minutes to obtain a homogeneous solution. The coating is carried out via doctor blading (15 mm/s at 60°C) under ambient conditions. The second PEDOT:PSS solution (Clevios HTL Solar) is applied via spin coater (30 s, 300 rpm/s, 2500 rpm).

- Preparation of the MoO_3 layer:

MoO_3 is applied by deposition at around $1 * 10^{-5}$ mbar (deposition chamber in glove box system MBraun LABmaster).

Silver is used as metal contact.

4.2. Device Fabrication for XPS and Contact Angle Measurements

The treatment of the ITO substrates, the preparation of the V_2O_5 as well as the TiO_X layer are the same for XPS and contact angle measurements as described above.

For the XPS measurements, the SAM coating is carried out via approach #2.

For the contact angle measurements, both preparations of the SAM layer are used.

4.3. Measuring Instruments

- For the contact angle measurements, the Krüss DSA 100 system was used.
- IV-Measurements were performed with a Keithley 2400 Sourcemeter (with a Deodlight 400 D using a LabViwe software) in a range of 1.5 V to 0.5 V

5. SUMMARY AND OUTLOOK

Organic photovoltaic devices have several advantages in contrast to solar cells of the first and second generation. Besides easy process technologies, organic compounds provide a huge range of properties with respect to the diverse possibilities of chemical structures.[12,13]

To generate electricity in OPV devices, excitons and their dissociation into electrons and holes are required.[12,14] The concentration of the free charge carriers, the transport of them to respective electrodes before recombination are determined through interfacial properties.[15,18] These qualities are important criteria for the performance of solar cells based on a donor acceptor blend. The insertion of self-assembling monolayers at interfaces is therefore a good possibility to control as well as to improve these properties.[45-61]

Electron and hole transport layers are well suited to be coated with SAMs.[45-61] SAMs can increase or decrease the work function of these layers, depending on the dipole moment of the respective molecules used.[46-48,50-55,60,61] Commonly used self-assembling molecules are benzoic acid and derivates thereof,[46,52-61] thiols[45-46] and phosphonic acids.[50-52]

Various studies show the positive effect of SAMs on the performance of solar cells:[45-61]

- Due to a better adaption of the work functions of the materials used, an increased short circuit current density as well as an enhanced voltage are obtained.
- The interfacial series resistance is lowered because of better charge collecting properties.
- By insertion of molecules with a hydrophobic nature, the wettability of the following photoactive layer and the morphology with respect to the size of the domains of donor and acceptor are improved.

In this thesis, the influence of benzoic acid, four para-substituted derivates thereof and two phosphonic acids on the performance of P3HT:PCBM based solar cells is investigated. Therefore, the normal (with V_2O_5 as a hole transport layer) and the inverted (with TiO_X as an electron transport layer) device architecture are used.

In the normal device architecture ITO/V_2O_5/P3HT:PCBM/Al, an efficiency improvement of about 65% (from 1.15% to 1.9%) using approach #1 is observed. In approach #2, the cell efficiency has more than doubled (from 1.15% to 2.5%). Here, all SAMs used show a positive effect on the PCE. Main reason for this improvement is the increased I_{SC} due to a higher concentration of free charge carriers.[53] Based on the V_{OC} values, there is no effect of the dipole moment of the SAMs used. The higher efficiency improvement of approach #2 can be explained by a more continuous coating of the SAMs on the V_2O_5 layer. This is also confirmed by the lower standard variance in the water contact angles.

In the inverted device architecture ITO/TiO_X/P3HT:PCBM/PEDOT:PSS/Ag, different results were obtained. Using approach #1, only the devices with MBA show an increased efficiency, which is comparable with the data from Kim et al.[60] In approach #2, CBA, tBBA and BA treated devices have better PCE values. However, it is difficult to make an accurate statement about the effect of the SAMs, since the coating with PEDOT:PSS was partially incomplete. In addition, the coating of TiO_X via doctor blading was also problematic, because of a non-uniform film thickness. This uneven TiO_X layer could also be a reason for the different contact angles of water. Due to these problems, MoO_3 as a hole transport layer and a vapor-deposited TiO_X was tested. By the use of these two new layers, an influence of the dipole moment of the SAMs used is observed. tBBA, BA and MBA having a negative dipole moment, increase the V_{OC} as well as the I_{SC}. The highest efficiency improvement (≈ 42%) was observed in MBA treated devices due to the fact, that MBA has the greatest dipolar moment. CBA and FBA (negative dipole moment) decrease the PCE. The coating method of TiO_X has not only influence on the characteristic solar cell parameters, it also effects the contact angle. Using the vapor deposited TiO_X, tBBA show the highest value of the water contact angle, whereas CBA, with a more polar end group the lowest value has.

Finally, two phosphonic acids were applied on TiO_X. Using tDPA, the coating of the following P3HT:PCBM layer was not possible. The devices with PBA show an efficiency improvement of 10%.

Based on the contact angle and the XPS data, the coating of the different buffer layers with the SAMs was not uniform. However, it could be shown that using a self-assembling monolayer is an easy and effective way to improve the solar cell efficiency. Nevertheless, it is necessary to analyze, how the effective dipole moment on the respective buffer layers is with respect to the influence of the work function and what impacts the SAMs on the crystallization process of the photoactive layer have. Therefore, further experiments with respect to the buffer layers, the solvent used, the coating techniques and also several surface analysis have to be carried out.

6. APPENDIX

6.1. Abbreviations

ABA	4-AminoBenzoic Acid
AFM	Atomic Force Microscopy
AM	Air Mass
BA	Benzoic Acid
BHJ	Bulk HeteroJunction
CBA	4-CyanoBenzoic Acid
CBC	4-ChloroBenzoylChloride
CBP	4-ChlorophenyldichloroPhosphate
ClAlPc	ChloroAluminium Phthalocyanine
CBS	ChloroBenzene-Sulfonyl chloride
CdTe	Cadmium Telluride
CIGS	CopperIndiumGalliumSelenide
CuPc	Copper Phthalocyanine
ETL	Electron Transport Layer
FBA	4-FluoroBenzoic Acid
FF	FillFactor
HOMO	Highest Occupied Molecular Orbital
HTL	Hole Transport Layer
I_{SC}	Short Circuit Current
ITO	IndiumTinOxide
IV	Current-Voltage
LUMO	Lowest Unoccupied Molecular Orbital
MBA	4-MethoxyBenzoic Acid
MeOH	Methanol
NBA	4-NitrBenzoic Acid
OPV	Organic PhotoVoltaic
P3HT	Poly-(3-HexylThiophene)
PBA	4PhosphonoButyric Acid

pCA	1-PyreneCarboxylic Acid
PCBM	[6,6]-Phenyl C_{61} Vutyric acid Methyl ester
PCE	Power Conversion Efficiency
PEDOT:PSS	Poly(3,4EthyleneDiOxyThiophene) PolyStyrene Sulfonate
PV	PhotoVoltaic
R_S	Series Resistance
SAM	Self-Assembling Monolayer
SubPc	boron SubPhthalocyanine
tBA	4(thiophen-2-yl) Benzoic Acid
tBBA	4-*tert*-ButylBenzoic Acid
tDPA	1-tetradecylphosphonic acid
TEM	TransmissionElectronMicroscopy
THF	TetraHydroFuran
TiO_X	Titanium Oxide
V_2O_5	VanadiumOxide
V_{OC}	Open Circuit Voltage
WF	Work Function
XPS	X-Ray Photoelectron Spectroscopy
ZnO	Zinc Oxide

6.2. List of Figures

6.3. List of Tables

6.4. List of References

1 http://www.eia.gov/forecasts/ieo/pdf/0484%282013%29.pdf, 02.08.2014

2 http://www.iea.org/publications/freepublications/publication/Solar_Energy_Perspectives2011.pdf, **02.08.2014**

3 http://www.epia.org/fileadmin/user_upload/Publications/GMO_2013_-_Final_PDF.pdf, **02.08.2014**

4 H.-G. Wagemann and H. Eschrich, Photovoltaik: Solarstrahlung und Hableitereigenschaften, Solarzellenkonzepte und Aufgaben, 2. Auflage, **2010**, Vieweg & Teubner Verlag, p: 3; ISBN: 978-3-8348-0637-6

5 K. Mertens, Photovoltaik: Lehrbuch zu Grundlagen, Technologie und Praxis, 2. Auflage, **2013**, Carl Hanser Verlag, p: 33; ISBN: 978-3-446-43410-3

6 D. M. Chapin, C. S. Fuller and G. L. Pearson, J. Appl. Phys.; **1954**, *25* (5), pp: 676-677

7 V. Wesselak and S. Voswinkel, Photovoltaik: Wie Sonne zu Strom wird, **2012**, Springer-Verlag Berlin Heidelberg, p: 5; ISBN: 978-3-642-24296-0

8 R. W. Miles, G. Zoppi and I. Forbes, Mater. Today; **2007**, *10* (11), pp: 20-27

9 G. Conibeer, Mater. Today; **2007**, *10* (11), pp: 42-50

10 R. F. Service, Science, **2011**, *332*, p: 293

11 http://www.heliatek.com/newscenter/latest_news/neuer-weltrekord-fur-organische-solarzellen-heliatek-behauptet-sich-mit-12-zelleffizienz-als-technologiefuhrer/?lang=en, **07.08.2014**

12 S. Günes, H. Neugebauer and N. S. Sariciftci, Chem. Rev.; **2007**, *107* (4), pp: 1324-1338

13 J.-M. Nunzi, C.R. Physique; **2002**, *3*, 523

14 A. J. Heeger, Adv. Mater.; **2014**, *26* (1), pp: 10-28

15 Ch. Winder, N. S. Sariciftci, J. Mater. Chem.; **2004**, *14* (7), pp: 1077-1086

16 B. Kraabel, C. H. Lee, D. McBranch, D. Moses, N. S. Sariciftci and A. J. Heeger, Chem. Phys. Lett.; **1993**, *213* (3-4), pp. 389-394

17 G. Yu, J. Gao, J. C. Hummelen, F. Wudl and A. J. Heeger, Science, **1995**, *270* (5243), pp: 1789-1791

18 G. Yu and A. J. Heeger, J. Appl. Phys.; **1995**, *78* (7), pp: 4510-4515

19 H. Hoppe, N. S. Sariciftci, J. Mater. Chem.; **2006**, *16*, pp: 45-61

20 C. A. Gueymard, D. Myers and K. Emery, Solar Energy, **2002**, *73* (6), pp: 443-467

21 Ch. J. Brabec, A. Cravino, D. Meissner, N. S. Sariciftci, T. Fromherz, M. T. Minse, L. Sanchez and J. C. Hummelen, Adv. Funct. Mater.; **2001**, *11* (5), pp: 374-380

22 M. C. Scharber, D. Mühlbacher, M. Koppe, P. Denk, Ch. Waldauf, A. J. Heeger and Ch. J. Brabec, Adv. Mater.; **2006**, *18* (6), pp: 789-794

23 J. Liu, Y. Shi, Y. Yang, Adv. Funct. Mater.; **2001**, *11* (6), pp: 420-424

24 J. C. Scott, S. A. Carter, S. Karg, M. Angelopoulos, Synth. Met.; **1997**, *85* (1-3), pp: 1197-1200

25 C. W. T. Bulle-Lieuwma, W. J. H. VanGennip, J. K. J. van Duren, P. Jankheijm, R. A. J. Janssen and J. W. Niemantsverdriet, Appl. Surf. Sci.; **2003**, *203-204*, pp: 547-550

26 H. Hoppe, T. Glatzel, M. Niggemann, W. Schwinger, F. Schaeffler, A. Hinsch, M. Ch. Lux-Steiner and N. S. Sariciftci, Thin Solid Films, **2006**, *511-512*, pp: 587-592

27 H. Kim, C. M. Gilmore, A. Piqué, J. S. Horwitz, H. Mattoussi, H. Murata, Z. H. Kafafi and D. B. Chrisey, J. Appl. Phys.; **1999**, *86* (11),pp: 6451-6461

28 J. Ouyang, CH.W. Chu, F.Ch. Chen, Q. Xu and Y. Yang, Adv. Fubct. Mater.; 2005, 15 (2), pp: 203-208

29 V. Shrotriya, G. Li, Y. Yao, C.-W. Chu and Y. Yang, Appl. Phys. Lett.; **2006**, *88* (07), pp: 073508-1-073508-3

30 J. Y. Kim, S. H. Kim, H.-H. Lee, K. Lee, W. Ma, X. Gong and A. J. Heeger, Adv. Mater.; **2006**, *18* (5), pp: 572-576

31 H. Schmidt, K. Zilberberg, S. Schmale, H. Flügge, T. Riedl and W. Kowalsky, Appl. Phys. Lett.; **2010**, *96* (24), pp: 243305-1-243305-3

32 C. Waldauf, M. Morana, P. Denk, P. Schilinsky, K. Coakley, S. A. Choulis and C. J. Brabec, Appl. Phys. Lett.; **2006**, *89* (23), pp: 233517-1-233517-3

33 Y. Udum, P. Denk, G. Adam, D. H. Apaydin, A. Nevosad, Ch. Teichert, M. S. White, N. S. Sariciftci and M. C. Scharber, Org. Electr.; **2014**, *15* (5), pp: 997-1001

34 X. Yang, J. Loos, S. C. Veenstra, W. J. H. Verhees, M. M. Wienk, J. M. Kroon, M. A. J. Michels and R. A. J. Janssen, Nano Lett.; **2005**, *5* (4), pp: 579-583

35 P. Vanlaeke, A. Swinnen, I. Haeldermans, G. Vanhoyland, T. Aernouts, D. Cheyns, C. Deibel, J. D`Haen, P. Heremans, J. Poortsmans and J. V. Manca, Sol. Energy Mater. And Sol. Cells, **2006**, *90* (14), pp: 2150-2158

36 T. J. Prosa, M. J. Winokur, J. Moulton, P. Smith and A. J. Heeger, Macromolecules, **1992**, *25* (17), pp: 4364-4372

37 H. Sirringhaus, N. Tessler and R. H. Friend, Science, **1998**, *280* (5370), pp: 1741-1744

38 V. D. Mihailetchi, J. K. J. Van Duren, P. W. M. Blom, J. C. Hummelen, R. A. J. Janssen, J. M. Kroon, M. T. Rispens, W. J. H. Verhees and M. M. Wienk, Adv. Funct. Mater; **2003**, *13* (1), pp: 43-46

39 X. Yang, J. K. J. Van Duren, M. T. Rispens, J. C. Hummelen, R. A. J. Janssen, M. A. J. Michels and J. Loos, Adv. Mater.; **2004**, *16* (9-10), pp: 802-806

40 J. Y. Kim, K. Lee, N. E. Coates, D. Moses, T.-Qu. Nguyen, M. Dante ans A. J. Heeger, Science, **2007**, *317* (5835), pp: 222-225

41 H. Kim, M. Shin and Y. Kim, Europhys. Lett.; **2008**, *84* (5), pp: 58002 – 28006

42 W.-H. Tseng, M.-H. Chen, J.-Y. Wang, Ch.-T. Tseng, H. Lo, P.S. Wang and Ch.i Wu, Sol. Energy Mater. and Sol. Cells; **2011**, *95* (12), pp: 3424-3427

43 S. S. van Bavel, M. Bärenklau, G. de With, H. Hoppe and J. Loos, Adv. Funct. Mater.; **2010**, *20* (9), pp: 1458-1463

44 W. Ma, C. Yang, X. Gong, K. Lee and A. J. Heeger, Adv. Funct. Mater.; **2005**, *15* (10), pp: 1617 – 1622

45 W. Chen, CH. Huang, X. Y. Gao, L. Wang, Ch. G. Zhen, D. Qi, S. Chen, H. L. Zhang, K. P. Loh, Z. K. Chen and A. T. S. Wee, J. Phys. Chem. B; **2006**, *110* (51), pp: 26075-26080

46 Hanène Bedis, JSEMAT, **2011**, *1*, pp: 42-50

47 X. Bulliard, S.-G. Ihn, S. Yun, Y. Kim, D. Choi, J.-Y. Choi, M. Kim, M. Sim, J.-H. Park, W. Choi and K. Cho, Adv. Funct. Mater.; **2010**, *20*, pp: 4381-4387D. K. Schwartz, Annu. Rev. Phys. Chem.; **2001**, *52*, pp: 107-137

48 J. S. Kim, J. H. Park, J. H. Lee, Appl. Phys. Lett.; **2007**, *91* (11), pp: 11211-1-3

49 M. Halik and A. Hirsch, Adv. Mater.; **2011**, *23*, pp: 2689-2695

50 M. Glibo, L. Sang, K. M. Knesting, M. C. Schalnat, A. Mudaligne, E. L. Ratcliff, H. Li, A. K. Sigdel, A. J. Giordano, J. J. Berry, D. Nordlund, G. T. Seidler, J. L. Bredas, S. R. Marder, J. E. Pemberton and D. S. Ginger, Langmuir; **2013**, *29*, pp: 2166-2174

51 J. D. Zimmermann, B. Song, O. Griffith and St. R. Forrest, Appl. Phys. Lett.; **2013**, *103* (24), pp: 243905-1-5

52 S. Khodabakhsh, B. M. Sanderson, J. Nelson and T. S. Jones, Adv. Funct. Mater.; **2006**, *16* (1), pp: 95-100

53 Ch. Goh, S. R. Scully and M. D. McGehee, J. Appl. Phys.; **2007**, *101* (11), pp: 114503-1-114503-12

54 H.-L. Yip, St. K. Hau, N. S. Baek, H. Ma and A. K.-Y. Jen, Adv. Mater.; **2008**, *20* (12), pp: 2376-2382

55 L. Macaraig, T. Sagaw and S. Yoshikawa, Energy Procedia; **2011**, *9*, pp: 283-291

56 St. Bastide, R. Butruille, D. Cahen, A. Dutta, J. Libman, A. Shanzer, L. Sun and A. Vilan, J. Phys. Chem. B; **1997**, *101* (14), pp: 2678-2684

57 S. Rühle, M. Greenstein, S.-G. Chen, A. Merson, H. Pizem, Ch. S. Sukenik, D. Cahen and A. Zaban, J. Phys. Chem. B; **2005**, *109* (40), pp: 18907-18913

58 G. Ashkenasy, D. Cahen, R. Cohen, A. Shanzer and A. Vilan, Acc. Chem. Res.; **2002**, *35* (2), pp: 121-128

59 F. Nüesch, M. Carrara and L. Zuppiroli, Langmuir; **2003**, *19* (12), pp: 4871-4875

60 Y. E. Ha, M. Y. Jo, J. Park, Y.-Ch. Kang, S. I. Yoo and J. H. Kim, J. Phys. Chemistry C; **2013**, *117*, pp:2646-2652

61 N. Beaumont, I. Hancox, P. Sullivan, R. A. Hatton and T. S. Jones, Energy Environ. Sci.; **2011**, *4*, 1708-1711

62 D. K. Schwartz, Annu. Rev. Phys. Chem.; **2001**, *52*, pp: 107-137

63 A. Ulman, Chem. Rev.; **1996**, *96* (4), pp: 1533-1554

64 F. Schreiber, Progr. In Surf. Science, **2000**, *65* (5-8), pp: 151-257

65 T.H. Lai, S.-W. Tsang, J. R. Manders, S. Chen and F. So, Materials Today, **2013**, *16* (11), pp: 424-432

66 I. D. Parker, J. Appl. Phys.; **1994**, *75* (3), pp: 1656-1666

67 J. S. Kim, F. Cacialli, M. Granström, R.H. Friend, N. Johansson, W. R. Salaneck, R. Daik and W. J. Feast, Synth. Met.; **1999**, *101* (1-3), pp: 111-112

68 A. C. Arias, L. S. Roman, T. Kugler, R. Toniolo, M. S. Meruvia, I. A. Hümmelgen, Thin Solid Films; **2000**, *371* (1-2), pp: 201-206

69 A. C. Arango, L. R. Johnson, V. N. Bliznyuk, Z. Schlesinger, S. A. Carter and H.-H. Hörhold, Adv. Mater.; **2000**, *12* (22), pp: 1689-1692

70 St. K. Hau. Y.-J. Cheng, H.-L. Yip, Y. Zhang, H. Ma and A. K.-Y. Jen, Appl. Mater. and Interf.; **2010**, *2* (7), pp: 1892-1902

71 M. Grätzel, Nature; **2001**, *414*, pp: 338-344

72 St. K. Hau, H.-L. Yip, O. Acton, N. S. Beak, H. Ma and A. K.-Y. Jen, J. Mater. Chem.; **2008**, *18*, pp: 5113-5119

73 Y. Yuan and T. R. Lee, Surface Sciene Technique, **2013**, Springer Verlag Berlin Heidelberg, , p: 3-5

74 N. Özer, Thin Solid Films, **1997**, *305*, pp: 80-87

75 A. K. Ghosh, Introduction to Measurements and Instrumentation, 3. Edition, **2009**, PHI Learning Private Limited, New Delhi, pp:623-624; ISBN: 978-81-203-3858-6

76 E. McCafferty and J. P. Wightman, Appl. Surf. Science; **1999,** *143* (1-4), pp: 92-100

77 X.-H. Guan, G.-H Chen and C. Shang, J of Environm. Sciences, **2007**, *19*, pp: 438-443

78 http://srdata.nist.gov/xps/Default.aspx, 01.10.2014

79 Dissertation R.Steim, The impact of Interfaces on the Performance of OPV, **2010**, KIT Scientific Publishing, ISBN: 978-3-86644-526-0

80 S. Chambon, L. Derue, M. Lahaye, B. Pavageau, L. Hirsch and G. Wantz, Materials; **2012**, *5*, pp: 2521-2536

81 Dissertation Ch. Fradler, Strategies to Improve the Efficiency of Hybrid Solar Cells; **2014**, TU Graz

6.5. XPS Data

Erläuterungen

In diesem Abschnitt sollen die im Bericht verwendeten Abkürzungen, Parameter und Einstellungen erklärt sowie allgemeine Informationen zu Messungen mit XPS gegeben werden.

Parameter und deren Bedeutung:

Die nachfolgenden Tabellen, Einstellungen und Parameter sind exemplarisch und ausschließlich zu Informationszwecken angeführt.

Experiment Descriptions Table

Exp1\X-Ray021 400um - FG ON\AA Mitte1

Exp1........lokaler Name der Experimentdefinitionsdatei

X-Ray021...Name eines Knotenpunkts in der Experimentdefinitionsdatei

400um.......Größe des verwendeten Röntgenflecks in µm

FG ON.......Flood Gun zum Ladungsausgleich während des Experiments eingeschaltet

AA............. Auto-Analyse – Identifizierung und Quantifizierung der Bestandteile durch die Software

Mitte1....... Bezeichnung des vermessenen Punktes

Common Acquisition Parameters Table

Parameter		***Erläuterung***
No. Scans	3	Anzahl der Wiederholungen je Einzelmessung
Source Type	Al K Alpha	Verwendete Röntgenstrahlung (typ. 1486.6eV)
Spot Size	400 µm	Größe des Röntgenflecks
Lens Mode	Standard	Modus des Linsensystems
Analyser Mode	CAE : Pass Energy 50.0 eV	Einstellung des Detektors
Energy Step Size	0.100 eV	Schrittweite bei Einzelscans

Bei der Auswertung und Quantifizierung der XPS-Messungen ist nach Literaturangaben von einem Fehler von rund 5% auszugehen.

In der Tabelle „Elemental ID and Quantification“ beschreibt:

Name:	die Bezeichnung des ausgewerteten Peaks
Peak BE:	die Position des Maximums des Peaks (eV)
Height Counts:	Counts am Peak-Maximum
FWHM eV:	die Halbwertsbreite des Peaks
Area (P) CPS. eV:	korrigierte Fläche unter der Kurve
At%:	Atomanteil in Prozent
Q:	gibt an ob der jeweilige Peak bei der Quantifizierung berücksichtigt wurde (1=ja; 0=nein)

Experiment Descriptions Table

Experiment\X-Ray158 300um - FG ON\Spot 2 #1

Common Acquisition Parameters Table

Parameter	
Source Gun Type	Al K Alpha
Spot Size	300 µm
Lens Mode	Standard

- V_2O_5 – Spot 1

Elemental ID and Quantification

Name	Peak BE	Height CPS	FWHM eV	Area (P) CPS.eV	Atomic %	Q
O1s	530.274	479424.86	2.718	1437911.42	59.22	1
V2p	517.109	389516.64	2.788	1500135.11	18.59	1
C1s	284.296	51333.72	3.204	196624.18	20.68	1
N1s	401.776	6561.61	1.522	24260.89	1.51	1

- V2O5 – Spot 2

Elemental ID and Quantification

Name	Peak BE	Height CPS	FWHM eV	Area (P) CPS.eV	Atomic %	Q
O1s	530.293	480501.83	2.702	1443984.66	58.15	1
V2p	517.102	390002.56	2.820	1542611.35	18.69	1
C1s	284.319	53432.99	3.186	203464.44	20.93	1
N1s	401.146	7886.28	3.577	36923.94	2.24	1

- V_2O_5 with BA – Spot 1

Elemental ID and Quantification

Name	Peak BE	Height CPS	FWHM eV	Area (P) CPS.eV	Atomic %	Q
C1s Scan A	284.207	12125.55	1.480	21024.72	16.83	1
C1s Scan B	288.626	897.82	2.451	2582.34	2.07	1
C1s Scan C	285.549	2299.98	2.230	6015.64	4.82	1
O1s Scan A	530.258	87099.66	1.190	121378.84	38.03	1
O1s Scan B	531.034	24971.97	1.637	47883.34	15.01	1
N1s Scan A	400.935	1001.89	3.516	4094.90	1.94	1
N1s Scan B	401.873	482.77	0.722	406.97	0.19	1
V2p3 Scan A	517.355	71873.30	1.751	147660.06	21.11	1

- V_2O_5 with BA – Spot 2

Elemental ID and Quantification

Name	Peak BE	Height CPS	FWHM eV	Area (P) CPS.eV	Atomic %	Q
C1s Scan A	284.202	12474.36	1.482	21659.13	17.31	1
C1s Scan B	288.668	1233.42	1.715	2480.64	1.99	1
C1s Scan C	285.719	2038.51	2.488	5942.73	4.75	1
O1s Scan A	530.206	85912.86	1.178	118495.17	37.09	1
O1s Scan B	530.969	27599.09	1.567	50681.35	15.87	1
N1s Scan B	401.254	946.45	3.236	3575.59	1.69	1
V2p3 Scan A	517.318	72588.60	1.752	149129.60	21.30	1

- V_2O_5 with CBA – Spot 1

Elemental ID and Quantification

Name	Peak BE	Height CPS	FWHM eV	Area (P) CPS.eV	Atomic %	Q
C1s Scan A	284.018	13344.58	1.421	22196.32	17.64	1
C1s Scan B	288.177	1206.50	1.678	2374.32	1.89	1
C1s Scan C	285.103	2853.40	2.635	8784.39	6.99	1
O1s Scan A	530.015	84790.78	1.222	121279.15	37.74	1
O1s Scan B	530.882	20422.30	1.783	42691.58	13.29	1
N1s Scan A	399.417	1257.38	2.083	3072.65	1.44	1
N1s Scan B	401.729	1038.91	1.826	2224.26	1.04	1
V2p3 Scan A	517.097	68453.56	1.751	140634.37	19.97	1

- V_2O_5 with CBA – Spot 2

Elemental ID and Quantification

Name	Peak BE	Height CPS	FWHM eV	Area (P) CPS.eV	Atomic %	Q
C1s Scan A	284.037	13138.52	1.384	21285.41	16.90	1
C1s Scan B	288.323	1189.04	1.568	2185.68	1.74	1
C1s Scan C	285.161	3096.93	2.414	8753.86	6.95	1
O1s Scan A	530.007	83223.13	1.184	115381.51	35.87	1
O1s Scan B	530.854	24223.94	1.740	49404.43	15.37	1
N1s Scan A	399.255	1253.74	2.341	3442.70	1.61	1
N1s Scan B	401.560	1123.17	1.972	2598.97	1.22	1
V2p3 Scan A	517.103	68371.12	1.788	143422.16	20.34	1

- V_2O_5 with FBA – Spot 1

Elemental ID and Quantification

Name	Peak BE	Height CPS	FWHM eV	Area (P) CPS.eV	Atomic %	Q
C1s Scan A	284.542	9851.12	1.497	17298.16	14.36	1
C1s Scan B	288.951	802.29	3.512	3286.41	2.73	1
C1s Scan C	285.914	2401.12	1.973	5556.03	4.62	1
O1s Scan A	530.545	86143.55	1.169	117912.37	38.32	1
O1s Scan B	531.242	30322.90	1.568	55683.21	18.11	1
N1s Scan A	401.054	770.03	3.519	3147.30	1.54	1
N1s Scan B	402.297	659.03	1.126	869.60	0.43	1
V2p3 Scan A	517.738	84225.51	1.359	134131.84	19.89	1

- V_2O_5 with FBA – Spot 2

Elemental ID and Quantification

Name	Peak BE	Height CPS	FWHM eV	Area (P) CPS.eV	Atomic %	Q
C1s Scan A	284.285	10249.36	1.477	17738.87	14.30	1
C1s Scan B	288.066	772.56	3.455	3117.24	2.52	1
C1s Scan C	285.351	4609.17	2.157	11657.03	9.40	1
O1s Scan A	530.303	85883.84	1.215	122239.19	38.59	1
O1s Scan B	531.156	19632.09	1.780	40964.73	12.94	1
N1s Scan A	400.973	959.47	3.518	3921.51	1.87	1
N1s Scan B	401.697	327.02	0.671	255.75	0.12	1
V2p3 Scan A	517.385	69943.56	1.715	140670.34	20.26	1

- V_2O_5 with MBA – Spot 1

Elemental ID and Quantification

Name	Peak BE	Height CPS	FWHM eV	Area (P) CPS.eV	Atomic %	Q
C1s Scan A	284.609	10879.28	1.431	18249.36	14.66	1
C1s Scan B	288.981	1025.95	1.752	2107.76	1.70	1
C1s Scan C	285.727	2811.62	2.451	8076.74	6.49	1
O1s Scan A	530.675	87452.96	1.201	123246.87	38.77	1
O1s Scan B	531.449	23039.32	1.789	48329.43	15.21	1
N1s Scan A	400.452	809.10	3.006	2849.47	1.35	1
N1s Scan B	402.162	643.00	2.414	1821.50	0.86	1
V2p3 Scan A	517.762	71019.17	1.751	145905.28	20.94	1

- V_2O_5 with MBA – Spot 2

Elemental ID and Quantification

Name	Peak BE	Height CPS	FWHM eV	Area (P) CPS.eV	Atomic %	Q
C1s Scan A	284.620	11530.95	1.457	19699.89	15.70	1
C1s Scan B	289.146	1033.58	1.973	2391.66	1.91	1
C1s Scan C	285.856	2562.01	2.672	8016.68	6.39	1
O1s Scan A	530.641	86938.94	1.200	122207.82	38.13	1
O1s Scan B	531.437	23078.45	1.752	47413.42	14.80	1
N1s Scan A	400.380	1012.15	1.862	2210.74	1.04	1
N1s Scan B	402.136	940.31	2.415	2663.75	1.25	1
V2p3 Scan A	517.762	71019.17	1.751	145905.28	20.77	1

- V_2O_5 with tBBA

Elemental ID and Quantification

Name	Peak BE	Height CPS	FWHM eV	Area (P) CPS.eV	Atomic %	Q
C1s Scan A	284.569	12232.92	1.424	20436.30	16.27	1
C1s Scan B	289.137	1214.25	1.916	2728.60	2.18	1
C1s Scan C	285.881	2591.40	2.377	7224.90	5.76	1
O1s Scan A	530.634	88598.02	1.219	126402.00	39.42	1
O1s Scan B	531.465	19989.08	1.862	43659.64	13.62	1
N1s Scan A	400.327	612.55	3.509	2501.73	1.18	1
N1s Scan B	402.123	544.26	2.709	1729.51	0.81	1
V2p3 Scan A	517.704	71031.31	1.751	145930.22	20.76	1

- V_2O_5 with tBBA – Spot 2

Elemental ID and Quantification

Name	Peak BE	Height CPS	FWHM eV	Area (P) CPS.eV	Atomic %	Q
C1s Scan A	284.297	12798.51	1.505	22574.91	18.19	1
C1s Scan B	288.752	1105.44	2.167	2810.12	2.27	1
C1s Scan C	285.926	2106.94	1.493	3686.81	2.97	1
O1s Scan A	530.330	88352.74	1.202	124383.98	39.24	1
O1s Scan B	531.155	22120.33	1.739	45088.17	14.23	1
N1s Scan A	399.984	906.65	2.034	2162.39	1.03	1
N1s Scan B	401.970	822.26	1.494	1440.34	0.69	1
V2p3 Scan A	517.412	72315.93	1.751	148569.41	21.39	1

- TiO_X – Spot 1

Elemental ID and Quantification

Name	Peak BE	Height CPS	FWHM eV	Area (P) CPS.eV	Atomic %	Q
Ti2p	458.808	414130.22	1.724	1831286.84	20.90	1
O1s	530.281	535357.83	2.938	1763379.32	56.74	1
C1s	285.078	61949.07	3.232	250982.52	20.63	1
Si2p	102.428	4767.23	1.403	12923.42	1.19	1
N1s	400.378	2974.99	3.743	10904.87	0.53	1

- TiO_X – Spot 2

Elemental ID and Quantification

Name	Peak BE	Height CPS	FWHM eV	Area (P) CPS.eV	Atomic %	Q
Ti2p	458.361	403841.26	1.732	1808324.34	20.73	1
O1s	530.224	524096.54	2.999	1736616.14	56.14	1
C1s	284.978	64769.74	3.333	269978.08	22.30	1
N1s	400.358	3353.80	3.561	16833.21	0.82	1

- TiO_X with BA – Spot 1

Elemental ID and Quantification

Name	Peak BE	Height CPS	FWHM eV	Area (P) CPS.eV	Atomic %	Q
C1s Scan A	285.022	9287.14	1.236	13439.09	9.60	1
C1s Scan B	289.174	2217.09	1.382	3595.98	2.57	1
C1s Scan C	285.853	11570.80	1.862	25272.94	18.05	1
O1s Scan A	530.480	93958.63	1.249	137466.07	38.43	1
O1s Scan B	531.877	16695.33	2.083	40796.42	11.41	1
N1s Scan A	400.283	320.67	1.236	464.62	0.20	1
Ti2p3 Scan A	459.020	87241.04	1.231	125691.71	18.89	1
N1s Scan B	401.065	495.38	3.519	2024.73	0.85	1

- TiO_X with BA – Spot 2

Elemental ID and Quantification

Name	Peak BE	Height CPS	FWHM eV	Area (P) CPS.eV	Atomic %	Q
C1s Scan A	284.455	18386.58	1.367	29442.97	21.09	1
C1s Scan B	288.398	2284.17	1.162	3112.48	2.23	1
C1s Scan C	285.674	1904.32	2.120	4735.26	3.39	1
O1s Scan A	529.717	101476.48	1.236	146842.99	41.17	1
O1s Scan B	531.088	16999.39	1.899	37861.29	10.63	1
N1s Scan A	400.592	511.30	3.513	2089.17	0.88	1
Ti2p3 Scan A	458.237	93784.81	1.224	134398.62	20.26	1
N1s Scan B	399.160	587.11	1.162	799.89	0.34	1

- TiO$_X$ with CBA – Spot 1

Elemental ID and Quantification

Name	Peak BE	Height CPS	FWHM eV	Area (P) CPS.eV	Atomic %	Q
C1s Scan A	285.467	11082.56	1.533	19916.88	13.91	1
C1s Scan B	289.201	1432.53	1.582	2656.27	1.86	1
C1s Scan C	286.868	2471.35	1.567	4542.82	3.18	1
O1s Scan A	530.663	123138.06	1.214	175240.04	47.92	1
O1s Scan B	531.981	14064.09	1.972	32543.45	8.91	1
N1s Scan A	400.124	1667.34	1.568	3064.89	1.26	1
Ti2p3 Scan A	459.279	107827.82	1.236	156234.63	22.96	1

- TiO$_X$ with CBA – Spot 2

Elemental ID and Quantification

Name	Peak BE	Height CPS	FWHM eV	Area (P) CPS.eV	Atomic %	Q
C1s Scan A	285.441	7351.28	1.309	11273.72	7.87	1
C1s Scan B	289.557	1408.82	1.494	2467.81	1.73	1
C1s Scan C	286.364	4104.76	2.304	11094.90	7.75	1
O1s Scan A	530.671	130662.15	1.194	182808.47	49.97	1
O1s Scan B	532.054	12816.07	1.899	28547.19	7.81	1
N1s Scan A	400.134	1574.31	1.677	3098.16	1.28	1
Ti2p3 Scan A	459.365	113660.41	1.205	160508.20	23.59	1

- TiO$_X$ with FBA -. Spot 1

Elemental ID and Quantification

Name	Peak BE	Height CPS	FWHM eV	Area (P) CPS.eV	Atomic %	Q
C1s Scan A	284.816	18612.05	1.374	29947.10	20.91	1
C1s Scan B	288.709	2081.89	1.310	3196.60	2.24	1
C1s Scan C	285.915	1674.89	2.856	5594.73	3.91	1
O1s Scan A	530.073	103570.56	1.198	145393.43	39.73	1
O1s Scan B	531.357	18890.25	1.862	41259.29	11.28	1
N1s Scan A	400.116	740.86	2.120	1842.49	0.76	1
N1s Scan B	402.208	276.83	0.918	297.37	0.12	1
Ti2p3 Scan A	458.627	94394.90	1.236	136771.31	20.09	1
F1s Scan A	687.433	2400.06	1.714	4827.00	0.97	1

- TiO$_X$ with FBA – Spot 2

Elemental ID and Quantification

Name	Peak BE	Height CPS	FWHM eV	Area (P) CPS.eV	Atomic %	Q
C1s Scan A	284.545	21326.23	1.384	34550.16	24.10	1
C1s Scan B	288.380	2840.23	1.313	4370.92	3.05	1
C1s Scan C	286.007	1814.12	2.378	5058.39	3.53	1
O1s Scan A	529.767	91532.96	1.199	128494.91	35.07	1
O1s Scan B	531.060	20920.46	2.009	49298.58	13.47	1
N1s Scan A	399.658	538.29	1.211	763.55	0.31	1
N1s Scan B	400.480	541.19	3.511	2211.00	0.91	1
Ti2p3 Scan A	458.350	84954.28	1.273	126767.00	18.60	1
F1s Scan A	687.210	2115.14	1.899	4711.38	0.95	1

- TiO_X with MBA – Spot 1

Elemental ID and Quantification

Name	Peak BE	Height CPS	FWHM eV	Area (P) CPS.eV	Atomic %	Q
C1s Scan A	284.073	7424.34	1.236	10743.50	7.54	1
C1s Scan B	287.763	1456.06	3.508	5961.53	4.19	1
C1s Scan C	284.908	9124.61	1.641	17545.18	12.32	1
O1s Scan A	529.236	120029.16	1.163	163306.17	44.86	1
O1s Scan B	530.839	9819.34	3.004	34295.43	9.43	1
N1s Scan A	399.144	242.43	1.336	379.51	0.16	1
Ti2p3 Scan A	457.996	110056.34	1.129	145571.62	21.50	1

- TiO_X with MBA – Spot 2

Elemental ID and Quantification

Name	Peak BE	Height CPS	FWHM eV	Area (P) CPS.eV	Atomic %	Q
C1s Scan A	284.106	8882.61	1.383	14406.98	10.03	1
C1s Scan B	285.648	3066.87	1.568	5631.82	3.93	1
C1s Scan C	288.276	1223.84	3.513	5013.60	3.50	1
O1s Scan A	529.243	135136.86	1.163	183861.01	50.11	1
O1s Scan B	530.643	9676.63	2.672	30140.26	8.22	1
N1s Scan A	398.745	234.86	1.251	344.41	0.14	1
N1s Scan B	400.488	159.44	2.262	422.90	0.17	1
Ti2p3 Scan A	458.021	122494.71	1.136	163026.99	23.89	1

- TiO_X with tBBA – Spot 1

Elemental ID and Quantification

Name	Peak BE	Height CPS	FWHM eV	Area (P) CPS.eV	Atomic %	Q
C1s Scan A	285.214	14103.16	1.384	22874.40	15.96	1
C1s Scan B	289.304	1246.14	3.508	5102.81	3.57	1
C1s Scan C	286.431	1971.85	0.903	2089.36	1.46	1
O1s Scan A	530.318	129704.40	1.163	176470.03	48.19	1
O1s Scan B	531.601	11171.80	2.046	26814.84	7.33	1
N1s Scan A	400.760	305.38	3.515	1248.03	0.51	1
Ti2p3 Scan A	459.086	114898.97	1.162	156540.77	22.98	1

- TiO_X with tBBA – Spot 2

Elemental ID and Quantification

Name	Peak BE	Height CPS	FWHM eV	Area (P) CPS.eV	Atomic %	Q
C1s Scan A	285.119	11245.66	1.299	17117.37	12.14	1
C1s Scan B	288.937	1480.14	1.327	2301.68	1.64	1
C1s Scan C	285.733	4138.93	1.862	9040.23	6.42	1
O1s Scan A	530.282	126234.57	1.162	171749.13	47.69	1
O1s Scan B	531.552	12713.02	2.083	31062.56	8.63	1
N1s Scan A	400.261	261.44	3.509	1067.75	0.45	1
Ti2p3 Scan A	459.029	113299.86	1.163	154362.12	23.04	1

- TiO$_X$ with tDPA – Spot 1

Elemental ID and Quantification

Name	Peak BE	Height CPS	FWHM eV	Area (P) CPS.eV	Atomic %	Q
Ti2p	458.795	412287.43	1.684	1879843.50	20.82	1
O1s	530.026	520688.83	2.780	1608910.59	50.23	1
C1s	284.912	106809.84	2.668	338411.61	27.00	1
P2p	133.176	9133.92	3.073	31166.70	1.94	1

- TiO$_X$ with tDPA – Spot 2

Elemental ID and Quantification

Name	Peak BE	Height CPS	FWHM eV	Area (P) CPS.eV	Atomic %	Q
Ti2p	458.313	458173.03	2.579	2005612.30	22.28	1
O1s	529.920	554158.29	2.736	1751671.23	54.86	1
C1s	284.842	78816.77	2.791	266242.13	21.31	1
P2p	133.109	6397.82	2.980	24854.14	1.55	1

- TiO$_X$ with PBA – Spot 1

Elemental ID and Quantification

Name	Peak BE	Height CPS	FWHM eV	Area (P) CPS.eV	Atomic %	Q
Ti2p	458.919	513897.97	2.574	2236780.15	24.66	1
O1s	530.144	636278.47	2.823	2019377.53	62.76	1
C1s	285.229	32389.82	3.097	138230.15	10.98	1
P2p	133.466	9189.92	2.625	25718.03	1.60	1

- TiO_X with PBA – Spot 2

Elemental ID and Quantification

Name	Peak BE	Height CPS	FWHM eV	Area (P) CPS.eV	Atomic %	Q
Ti2p	458.920	508163.86	2.574	2230870.40	24.89	1
O1s	530.144	631359.81	2.834	2000239.88	62.90	1
C1s	285.200	33787.49	3.043	134367.19	10.80	1
P2p	133.295	9522.67	1.987	22487.80	1.41	1